

AN ABSTRACT OF THE THESIS OF

Mohanalakshmi Koteeswaran for the degree of Master of Science in

Electrical and Computer Engineering presented on September 16, 2002.

Title: Substrate Coupling Macromodels for Lightly Doped CMOS Processes

Abstract approved: — **Redacted for privacy** —

Kartikeya Mayaram

Terri Fiez

A scalable macromodel for substrate noise coupling in lightly doped substrates with and without a buried layer has been developed. This model is based on Z -parameters and is scalable with contact size and separation. This model requires process dependent parameters that can be extracted easily from a small number of device simulations or measurements. Once these parameters are known, the model can be used for any spacing between the injecting and sensing contacts and for different contact geometries. The model is validated with measurements for a lightly doped substrate with a buried layer and predicts the substrate resistance values to within 12%. The substrate resistances obtained using the model are also in close agreement with the three-dimensional simulations for a lightly doped substrate.

©Copyright by Mohanalakshmi Koteeswaran

September 16, 2002

All rights reserved

Substrate Coupling Macromodel
for Lightly Doped CMOS Processes

by

Mohanalakshmi Koteeswaran

A THESIS

submitted to

Oregon State University

in partial fulfillment of
the requirements for the
degree of

Master of Science

Presented September 16, 2002
Commencement June 2003

Master of Science thesis of Mohanalakshmi Koteeswaran presented on
September 16, 2002

APPROVED:

Redacted for privacy

Major Professor, representing Electrical and Computer Engineering

Redacted for privacy

Head of the Department of Electrical and Computer Engineering

Redacted for privacy

Dean of the Graduate School

I understand that my thesis will become part of the permanent collection of Oregon State University libraries. My signature below authorizes release of my thesis to any reader upon request.

Redacted for privacy

Mohanalakshmi Koteeswaran, Author

ACKNOWLEDGMENTS

A lot of people have played a very important role in my reaching the stage of a graduate student. I would like to thank all my teachers and professors who have contributed to my academic growth. I would especially like to thank my advisors, Dr. Karti Mayaram and Dr. Terri Fiez for supporting this research and for their guidance, teaching, advice and constant support over the past two years. I also thank them for giving me the opportunity to work in a challenging and thought provoking environment. I would like to thank Dr. Michael Quinn and Prof. Roger Traylor for taking interest in my work and for taking the time to serve on my defense committee.

I would like to thank CDADIC and Teradyne and Semiconductor Research Corporation(SRC) for supporting this and related work and Teradyne for helping with the layout and fabrication of the test chip and for providing measured data. I also thank the various industry members who have contributed to my research through their feedback at CDADIC.

I would like to thank Cheng-gang Xu for his help with his software EPIC and Jose Silva for all the time he spent helping with the Cadence tools. I thank Ferne Simendinger for all her help especially at my arrival in the US.

The years I have spent in Oregon State University have been some of the most educational and enjoyable ones. I am very grateful to Dicle Ozis, Aline Sadate and Kannan Soundarapandian for their very helpful contributions to my research.

I would like to thank my friends Reshma Dixit, Kannan, Prashanth Drakshapalli, Raghuram Jonnalagedda, Nilakantan Seshan, Nathen Barton, Krishna

Prasad, Ajith Sharma, Ranganathan Desikachari, Manu Mishra, Sachin Ranganthan, Ravikanth Suravarapu, Manas Behera, Vivek Sharma, Thirumalai Rangachari, Goutham, Sirisha, Vinay Ramyeed and Ragini Murugan for all the support, encouragement, advice and fun. I would like to thank Prashanth, Thirumalai and Sachin for the rides at odd times of the night.

I am thankful to all my teachers and friends in my life. I am greatly indebted to my parents and my sister for their unwavering faith in my abilities and their support and help through my life. Their encouragement, guidance, love and sacrifices have been the main reason I have come this far. I also thank my grandparents for their unconditional love, support and many blessings.

TABLE OF CONTENTS

	<u>Page</u>
1 INTRODUCTION.....	1
2 BACKGROUND	4
3 MACROMODEL FOR TWO CONTACTS	7
3.1 Introduction.....	7
3.2 Resistive Substrate Network	9
3.3 Analysis of Lightly Doped Substrate With Buried Layer.....	11
3.4 Analysis of Lightly Doped Substrate Without a Buried Layer	15
3.5 Z-Parameter Based Model.....	18
3.6 Extending the Model to Multiple Contacts.....	19
4 EXTENSION OF THE MACROMODEL TO THE THIRD DIMENSION .	26
4.1 Introduction	26
4.2 3D Model of Lightly Doped Substrate Without a Buried Layer	27
4.3 3D Model of Lightly Doped Substrate With a Buried Layer	38
4.4 Coupling due to Multiple Interacting Sides.....	42
5 MEASUREMENT RESULTS.....	54
6 TECHNIQUES FOR IMPROVING ISOLATION	66
7 COMPARISON OF LIGHTLY DOPED AND HEAVILY DOPED PRO- CESSES.....	76

TABLE OF CONTENTS (Continued)

	<u>Page</u>
8 CONCLUSION	81
BIBLIOGRAPHY	82
APPENDICES.....	84
APPENDIX A Model Parameter Extraction for Z_{11}	85
APPENDIX B Model Parameter Extraction for Z_{12}	88

LIST OF FIGURES

<u>Figure</u>	<u>Page</u>
1.1 Noise injection mechanisms in an inverter.	2
2.1 Resistive model for the substrate for two contacts.	6
3.1 Cross-section of a lightly doped substrate without a buried layer. ...	7
3.2 Cross-section of a lightly doped substrate with a buried layer.	8
3.3 $1/G_{12}$ versus separation between two point contacts of $0.5 \mu m$	12
3.4 Comparison of the model for conductance G_{12} with MEDICI simulations for a lightly doped substrate with a buried layer.	12
3.5 Comparison of the model for conductance G_{11} with MEDICI simulations for a lightly doped substrate with a buried layer.	13
3.6 Comparison of the model for conductance G_{11} with MEDICI simulations for a lightly doped substrate without a buried layer.	15
3.7 Comparison of the model for conductance G_{12} with MEDICI simulations for a lightly doped substrate without a buried layer.	16
3.8 Resistance network for (a) two identical contacts (b) three identical contacts.	18
3.9 Z_{11} versus contact width in a lightly doped substrate with a buried layer.	21
3.10 $\frac{1}{Z_{11}}$ varies linearly with contact width in a lightly doped substrate with a buried layer.	21
3.11 Z_{11} versus contact width in a lightly doped substrate without a buried layer.	22
3.12 $\frac{1}{Z_{12}}$ versus contact width in a lightly doped substrate without a buried layer.	23
3.13 Z_{12} versus contact width in a lightly doped substrate with and without a buried layer.	24
4.1 Two-dimensional and three-dimensional views of substrate contacts. .	26
4.2 Z_{11} as a function of separation.	27

LIST OF FIGURES (Continued)

<u>Figure</u>	<u>Page</u>
4.3 Effect of nearby contacts on Z_{11}	28
4.4 The Z_{11} model is in good agreement with SCA simulations.	29
4.5 Z_{12} versus separation.	30
4.6 Z_{12} versus separation for $1\mu m \times 1\mu m$ contacts.	32
4.7 α as a function of the perimeter of the merged contacts.	33
4.8 ϵ as a function of the perimeter of the merged contacts.	33
4.9 An example of two contacts with different sizes.	34
4.10 Simulations and model for Z_{12} show a good agreement for non- identical contacts when $y=0$	35
4.11 Simulations and model for Z_{12} show a good agreement for non- identical contacts when $x = 30\mu m$	36
4.12 a_1 versus separation x	38
4.13 Comparison of the model for Z_{12} with SCA-3D simulations.	39
4.14 Simulations and the model for Z_{11} show good agreement.	40
4.15 Simulations and the model for Z_{12} for a lightly doped substrate with a buried layer show good agreement.	42
4.16 Simulations and the model for Z_{12} show good agreement for non- identical contacts for $y=0$	43
4.17 Simulations and model for Z_{12} show a good agreement for non- identical contacts for $x = 30\mu m$	43
4.18 Simulations and the model for Z_{12} show good agreement for non- identical contacts.	44
4.19 An L-shaped contact surrounding the square contact on two sides. . . .	45
4.20 Z_{12} due to the two sections A and B of the L-shaped contact and overall Z_{12} (C).	46

LIST OF FIGURES (Continued)

<u>Figure</u>	<u>Page</u>
4.21 The model is in good agreement with simulations for the structure in Fig. 4.19 for different x_0 values.	47
4.22 Movement of the small contact along a constant contour line shown in Fig. 4.24.	47
4.23 3D plot showing the coupling between the two contacts in Fig. 4.19... ..	48
4.24 Constant Z_{12} contour lines for the L-shaped contact and the square contact case.	49
4.25 U-shaped contact surrounding the square contact on three sides.	49
4.26 The model shows good agreement with simulated data for the geometry shown in Fig. 4.25.	50
4.27 Simulated data versus model for Z_{12} for the structure shown in Fig. 4.25 for $x = 30\mu m$	50
4.28 The square contact surrounded by another contact on all sides.	51
4.29 3D plot of Z_{12} for the geometry shown in Fig. 4.28.	51
4.30 Model shows good agreement with simulations of Z_{12} for the geometry shown in Fig. 4.28 for $x_0 = 50\mu m$	52
5.1 Layout of test structures.	55
5.2 Simulation setup to evaluate R_{1-4}	56
5.3 Array structure of $5\mu m \times 5\mu m$ contacts.	56
5.4 The two contacts are merged together to evaluate α and β	58
5.5 Comparison of measured resistance values with the model for the test structure shown in Fig. 5.3.	59
5.6 Array structure of $0.88\mu m \times 0.88\mu m$ contacts.	60
5.7 Comparison of measured resistance values with the model for the test array shown in Fig. 5.6.	61
5.8 Test structure 3 of $5\mu m \times 5\mu m$ contacts.	61

LIST OF FIGURES (Continued)

<u>Figure</u>	<u>Page</u>
5.9 Comparison of measured resistance values with the model for the test structure shown in Fig. 5.8.	63
5.10 Test structure 4 of $5\mu m \times 5\mu m$ contacts.	63
5.11 Comparison of measured resistance values with model for the test structure shown in Fig. 5.10.	64
5.12 Test structure 5 of $5\mu m \times 5\mu m$ contacts.	64
6.1 The effect of separation between injector and sensor on the isolation. .	66
6.2 Simulation setup to determine isolation.	67
6.3 Current flow lines illustrate nearby contact effects in a doped heavily substrate.	68
6.4 Isolation versus separation x with the guard ring and backplane grounded.	69
6.5 Setup with two guard rings.	70
6.6 Isolation versus separation x with the guard rings and backplane grounded for the structure shown in Fig. 6.5.	70
6.7 Setup with two guard rings around the sensor.	71
6.8 Isolation versus separation x with the guard rings and backplane grounded for the structure shown in Fig. 6.7.	72
6.9 Simulation setup used to evaluate the effect of the width of the guard ring on isolation.	72
6.10 Isolation versus width W of the guard ring.	73
6.11 Comparison of isolation obtained while using a grounded guard ring and guard ring with inductive impedance at different frequencies.	73
6.12 Comparison of isolation obtained while using a floating backplane, grounded backplane and pin inductance are shown.	74
7.1 Cross-section of a lightly doped substrate without a buried layer. ...	76

LIST OF FIGURES (Continued)

<u>Figure</u>		<u>Page</u>
7.2	Cross-section of a heavily doped substrate.	77
7.3	Resistive model of a lightly/heavily doped substrate.	77

LIST OF TABLES

<u>Table</u>	<u>Page</u>
3.1 Resistance values obtained from MEDICI simulations for a lightly doped substrate with and without the buried conductive layer.	10
3.2 A comparison of the simulated results with the model used to predict the resistance values of the substrate network.	14
3.3 A comparison of the simulated results with the model used to predict the resistance values of the substrate network for a lightly doped substrate without the buried layer.	17
3.4 Summary of equations and parameters extracted for the two lightly doped processes.	25
4.1 Summary of equations and parameters extracted for the two lightly doped processes.	53
5.1 Comparison of resistance values from 2D and 3D simulators with measured data for the test array shown in Fig. 5.3.	56
5.2 Comparison of resistance values from 2D and 3D simulators with measured data for the test array shown in Fig. 5.6.	60
5.3 Comparison of resistance values from 2D and 3D simulators with measured data for the test structure shown in Fig. 5.8.	62
5.4 Comparison of resistance values from 2D and 3D simulators with measured data for the test structure shown in Fig. 5.10.	62
5.5 Comparison of resistance values from 2D and 3D simulators with measured data for the test structure shown in Fig. 5.12.	65
7.1 Resistance values obtained from MEDICI simulations for lightly doped and heavily doped processes.	78
7.2 Comparison of isolation values obtained for different processes.	79

SUBSTRATE COUPLING MACROMODELS FOR LIGHTLY DOPED CMOS PROCESSES

1. INTRODUCTION

Advancements in communications and networking technologies have created a great demand for compact and portable mixed-signal circuits that integrate analog, RF, and digital circuits on a common silicon substrate. The integration of digital, analog and RF circuits on a single chip yields a "System on a Chip" (SOC) solution. There are several advantages and disadvantages to SOC solutions. The advantages are reduced size, lower cost and lower power dissipation. However, a major disadvantage of integration is the increased interaction between the high speed, noise-generating digital circuits and the analog circuits through the shared silicon substrate. This noise coupling can degrade the performance of the sensitive analog and RF circuits. The noise coupling can be eliminated by improved circuit design [1, 2], and by using special processes for ICs [3, 4]. However, in order to get a better understanding of the noise coupling through the substrate, the behavior of the substrate needs to be carefully understood.

Some of the noise injection and sensing mechanisms are discussed here briefly. The noise injection mechanisms in a MOS transistor are due to the junction capacitances formed by the source and drain regions with the substrate and the capacitance between the gate and the bulk. Fig. 1.1 shows the cross section of the layout of an in-

verter, a digital noise injector and the different junction capacitances are illustrated. Noise injection also occurs due to bond wire inductance. The switching operation

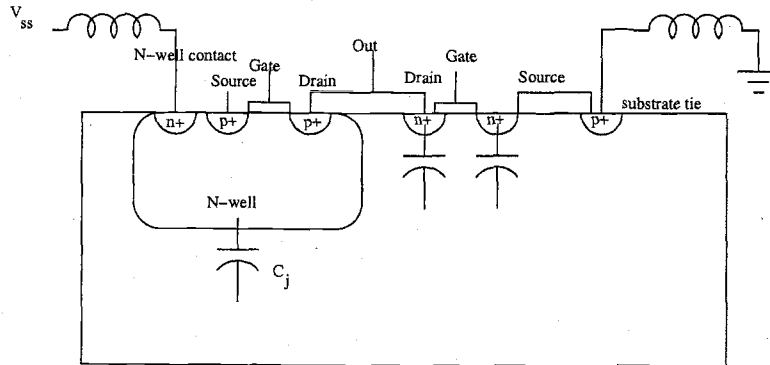


Figure 1.1. Noise injection mechanisms in an inverter.

of the inverter creates current spikes. Due to the current spikes and the wire inductances a $L \frac{di}{dt}$ voltage drop causes the V_{ss} node to have a voltage different from ground. This “ground bounce” injects a noise current into the substrate. The reception of noise in NMOS transistors occurs because of the junction capacitances [7], a significant mechanism at high frequencies. In PMOS transistors, noise is coupled through the junction capacitance C_j . Another significant mechanism of coupling in MOS transistors is the threshold voltage modulation due to the substrate noise. The change in threshold voltage causes a change in the drain current of the transistor.

Substrate noise coupling has been analyzed in several studies previously and a number of numerical techniques have been developed to characterize the noise coupling through the substrate [5-7]. However, these techniques can only be applied after the final layout is done or involve a computationally expensive model. An

alternative approach is to use a simple and intuitive macromodel that efficiently represents the substrate resistive network [8-11].

In this thesis, the focus is on noise coupling in lightly doped substrates and the isolation techniques that can be employed in these substrates. An efficient macromodel for multiple contacts has been developed for lightly doped substrates. This model can be used to evaluate noise coupling in the early stages of design and has been validated with both device simulations, substrate parasitic extraction tools, and measured data.

The organization of the thesis is as follows. Chapter 2 reviews some of the numerical methods used to generate a substrate model. Additionally, the macro-modeling approach is also described. A substrate coupling macromodel for lightly doped substrates is presented in Chapter 3. This model is then extended to the third dimension to make it scalable with the size and shape of contacts in Chapter 4. Chapter 5 deals with the validation of the proposed model through measurement results from a test chip. Isolation techniques are discussed in Chapter 6 which also provide guidelines on the placement of guard rings. The behavior of a heavily doped substrate is compared with that of a lightly doped substrate in Chapter 7. Conclusions and future work are presented in Chapter 8.

2. BACKGROUND

Prior work in substrate noise coupling problems has mostly focused on extracting the substrate model using detailed numerical analyses. This involves a trade-off between accuracy and simulation time. Some of the techniques that have been proposed for the extraction of the substrate network are discussed here.

In [12, 13], the substrate network is obtained using the finite difference method where the entire substrate is divided into a fine mesh. In order to simulate current flow and potentials in the substrate, device simulators were used. In this method, a simplified substrate equation is obtained from the Poisson's and current continuity equations. When the discretized version of the divergence theorem is substituted into the simplified substrate equation, a complex substrate network consisting of resistors and capacitors is obtained. Even though the finite difference method is applicable to any substrate, it is computationally expensive as its accuracy is directly related to the size of the mesh used.

The boundary element method is another popular technique used to obtain the substrate resistive network [5, 12]. This method makes use of Green's theorem applied to Laplace's equation, with appropriate boundary conditions. Here only the boundary surfaces are discretized, thus generating small but dense matrices. The method can be computationally expensive since a dense Z-matrix has to be inverted in order to obtain the resistive substrate network.

Another method to obtain the substrate network is the preprocessed boundary element method described in [6]. In [6], precomputed Z-parameters are used to generate the substrate network. Here, the cross-coupling Z-parameter Z_{ij} is expressed as a function of distance. The parameters for this function are obtained by

polynomial curve-fitting. The method is simple and for a given process the parameters can be extracted either from device simulations or measurements and stored in a library. The disadvantage with this method is that an exhaustive library has to be generated each time the technology is changed. Also, since the Z-parameters do not scale with the contact size, large contacts have to be discretized into panels before generation of the Z matrix. Therefore, this method can be computationally expensive.

All of the above methods can only be employed after the layout is complete and each one is either computationally expensive or requires libraries that have to be updated each time the technology is changed.

An alternative method of using a macromodel scalable with separation and contact size for a heavily doped process was proposed in [8, 11]. This work was extended to a macromodel for multiple contacts in [10]. By using the scalable macromodel approach, it is possible to extract the substrate resistance network for any contact dimensions or separations from a single model. When the layout is changed, the network is easily updated.

In [8, 9], the scalable model was developed for a two contact case using the 2-dimensional device simulator TMA-MEDICI [14]. The model proposed in [9] for a lightly doped process is a simple pi resistive network for low frequencies. The resistive model for two contacts is shown in Fig. 2.1. The source and sensor are P+ contacts separated by a distance x . The 2-port circuit consists of a coupling resistor, R_{12} , and two resistors to the backplane.

The advantage of the scalable macromodel is that it provides a very simple and accurate method to determine the substrate resistances and can be applied to

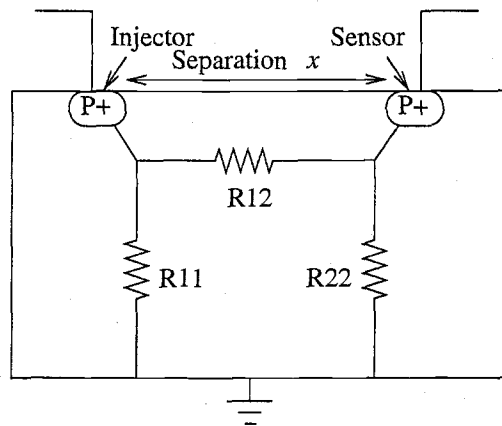


Figure 2.1. Resistive model for the substrate for two contacts.

different situations with little change. Substrate coupling between the digital and analog portions of a circuit can be determined before the final layout of the design, thus saving extensive simulation and redesign.

3. MACROMODEL FOR TWO CONTACTS

3.1. Introduction

In this chapter, a two-dimensional macromodel is developed for a two contact case in order to understand the effect of substrate coupling in lightly doped substrates. Two types of lightly doped substrates are analyzed here: one with a buried layer and another without a buried layer. Shown in Figs. 3.1 and 3.2 are the cross-sections of a lightly doped substrate without a buried layer and with a buried layer, respectively. A lightly doped substrate without a buried layer has two distinct layers: a lightly doped bulk and a more heavily doped P+ channel-stop implant. The doping information and the thicknesses for these layers are shown in Fig. 3.1. In the substrate with a buried layer, an additional heavily doped buried layer is included as shown in Fig. 3.2.

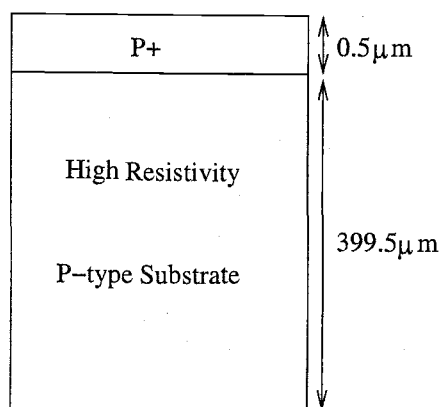


Figure 3.1. Cross-section of a lightly doped substrate without a buried layer.

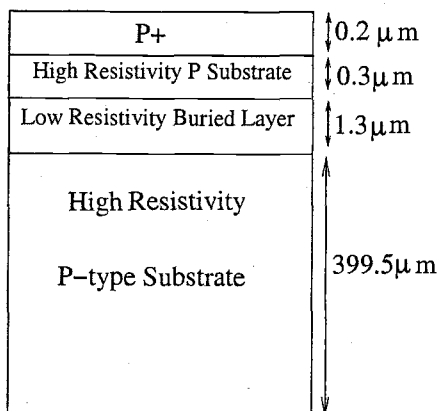


Figure 3.2. Cross-section of a lightly doped substrate with a buried layer.

In order to derive the model, the two-dimensional (2D) device simulator TMA-MEDICI was used. MEDICI allows the definition of non-homogeneous substrate layers and as a result it can be used for any substrate. An example of non-homogeneous substrate is a combination of regions with and without buried layers. MEDICI also gives a good understanding of the coupling mechanisms since one can plot the actual current flowing in the substrate. A device simulator can provide a good understanding of the substrate noise coupling mechanisms since the simulator allows for a number of different experiments such as changing width and separation between contacts.

The information supplied to MEDICI includes the process information such as the doping concentrations and layer thicknesses, the dimensions of the contacts, the substrate depth and the separation between the injecting and the sensing contacts.

MEDICI can be used to determine the Y or Z parameters. One can also obtain information about the current flow in the substrate.

3.2. Resistive Substrate Network

At frequencies below 1 GHz, the substrate can be modeled as a resistive network [8]. When the injector and sensor have the same doping concentration and dimensions the vertical resistances R_{11} and R_{22} between the contact and backplane are equal. The two port y-parameters are extracted from MEDICI for different simulation setups and the conductance network and resistance values are calculated as follows:

$$Y = \begin{bmatrix} y_{11} & y_{12} \\ y_{21} & y_{22} \end{bmatrix} = \begin{bmatrix} G_{11} + G_{12} & -G_{12} \\ -G_{21} & G_{21} + G_{22} \end{bmatrix}$$

Therefore,

$$G_{12} = -y_{12}$$

$$R_{12} = \frac{1}{-y_{12}}$$

The vertical resistance and the cross coupling resistance for the two substrate profiles, with and without the buried layer as separation x between the injector and the sensor varies, are shown in Table 3.1.

A comparison of the data shown in Table 3.1 shows that the cross-coupling resistance R_{12} is much greater for a lightly doped substrate without a buried layer than R_{12} for a lightly doped substrate with a buried layer. This is because the heavily doped region in the substrate in the latter case provides a low resistivity

Table 3.1. Resistance values obtained from MEDICI simulations for a lightly doped substrate with and without the buried conductive layer.

Separation (μm)	R_{11} (K Ω)		R_{12} (K Ω)	
	With BL	Without BL	With BL	Without BL
10	906	1574	5.09	36.8
20	636	487	7.72	50.3
30	531	319	10.3	65.2
40	386	241	12.8	88.5
50	312	205	15.3	110.4
60	293	189	17.8	131.4
70	270	175	20.2	152
80	245	155	22.7	172.4
90	227	139	25.2	192.5

path for the current to flow and the resistance between the injector and the sensor is reduced.

In order to understand the mechanism of noise coupling, the dependence of conductances G_{11} (conductance from the injector to the bulk), and G_{12} (cross coupling conductance between the contacts) on separation x between the contacts are examined first.

3.3. Analysis of Lightly Doped Substrate With Buried Layer

A lightly doped substrate with the buried layer shown in Fig. 3.2 is analyzed here. Figure 3.3 shows that $1/G_{12}$ increases linearly as the contact separation increases. Hence, G_{12} can be expressed as:

$$G_{12} = \frac{1}{a + bx} \quad (3.1)$$

where a and b are process dependent parameters that are obtained from curve fitting measured or simulated data. The values obtained for the simulated substrate profile are:

$$a = 2.56 \times 10^3 \, \Omega \quad b = 2.55 \times 10^8 \, \frac{\Omega}{m}$$

The plot of G_{12} in Fig. 3.4 shows a good agreement between the model of (3.1) and the data obtained from MEDICI simulations.

The variation of G_{11} in Fig. 3.5 with separation shows a flattening of the curve for large separations. Hence G_{11} can be expressed as a first order linear expression with a dependence on the square root of separation:

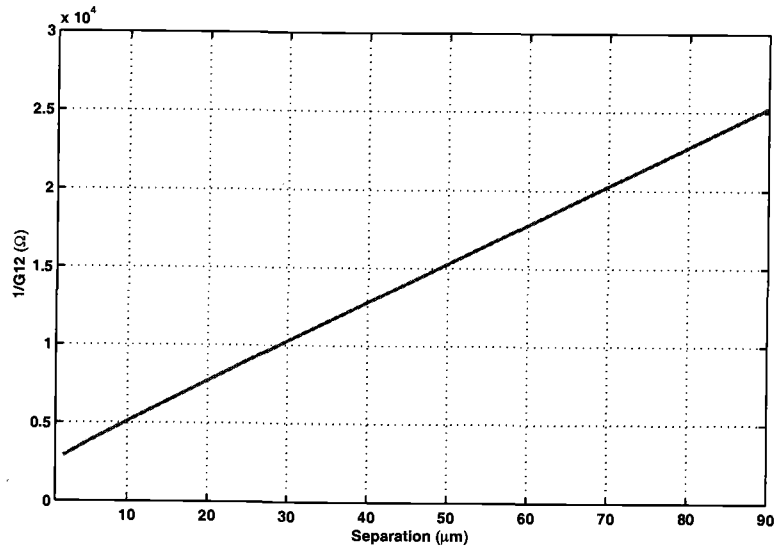


Figure 3.3. $1/G_{12}$ versus separation between two point contacts of $0.5 \mu\text{m}$.

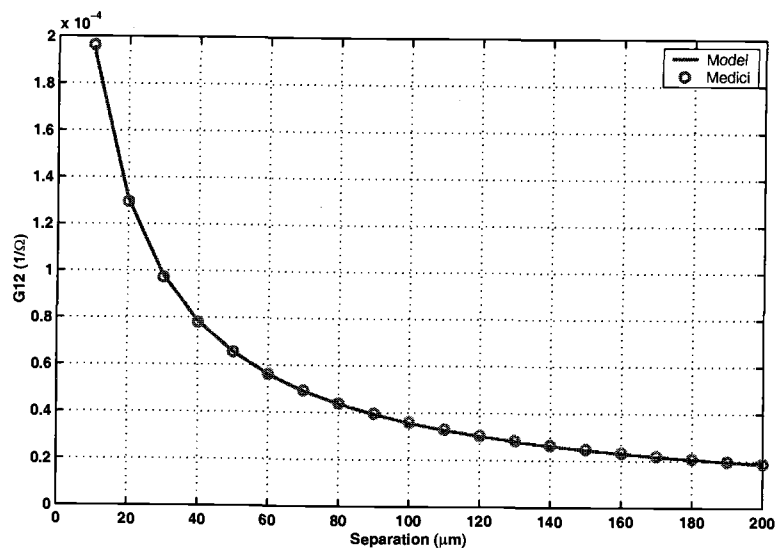


Figure 3.4. Comparison of the model for conductance G_{12} with MEDICI simulations for a lightly doped substrate with a buried layer.

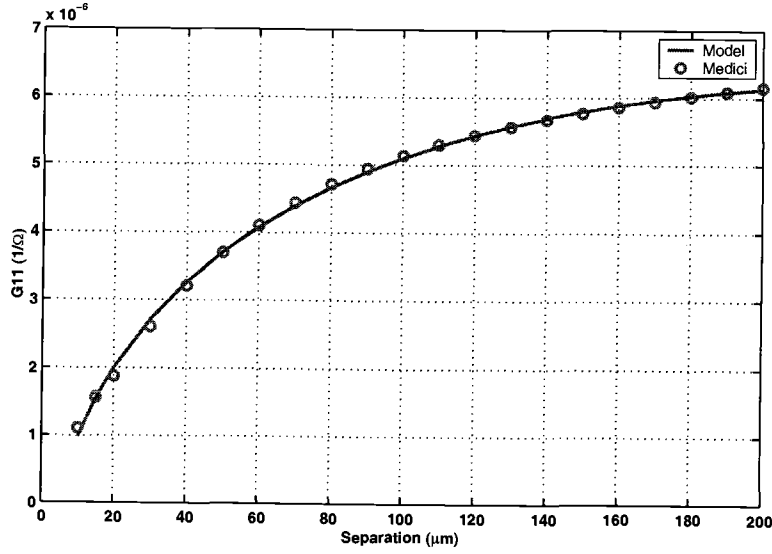


Figure 3.5. Comparison of the model for conductance G_{11} with MEDICI simulations for a lightly doped substrate with a buried layer.

$$G_{11} = \alpha + \beta x + \epsilon \sqrt{x} \quad (3.2)$$

where α , β and ϵ are process dependent parameters obtained from curve fitting the data. For this particular substrate doping, the values of these parameters are given by:

$$\alpha = -1.9 \times 10^{-6} \frac{1}{\Omega} \quad \beta = -3.21 \times 10^{-2} \frac{1}{\Omega m} \quad \epsilon = 1.024 \times 10^{-3} \frac{1}{\Omega \sqrt{m}}$$

The plot of G_{11} in Fig. 3.5 shows a good agreement between the model of (3.2) and the data extracted from MEDICI simulations. The model derived for G_{11} is only valid for separations greater than $10\mu m$.

The next step is to validate the model by comparing the values of cross-coupling resistances obtained from the model with simulated values. Resistance values are obtained from the Y parameters extracted from simulations as described earlier. The resistance values calculated from the two-port Y -matrix and the resistances obtained by using the model are tabulated in Table 3.2.

Table 3.2. A comparison of the simulated results with the model used to predict the resistance values of the substrate network.

Separation (μm)	R_{11} (K Ω)		R_{12} (K Ω)		<i>RelativeError</i>	
	Model	Sim.	Model	Sim.	R_{11}	R_{12}
10	1009	906	5.12	5.09	11%	0.58%
20	644	636	7.67	7.72	1.5%	0.65%
30	499	531	10.2	10.1	2.82%	0.39%
40	368	386	12.8	12.8	3.36%	0.15%
50	306	312	15.3	15.0	1.12%	0.32%
70	270	270.5	20.41	20.49	0.09%	0.39%
80	243	245	23.0	23.8	0.81%	0.05%
90	225	227	25.16	25.56	0.88%	0.23%

A comparison of the data in the Table 3.2 shows that the worst case error for the vertical resistance R_{11} is 11% for a separation of $10\mu m$ and the worst case error for the cross-coupling resistance R_{12} is less than 1%.

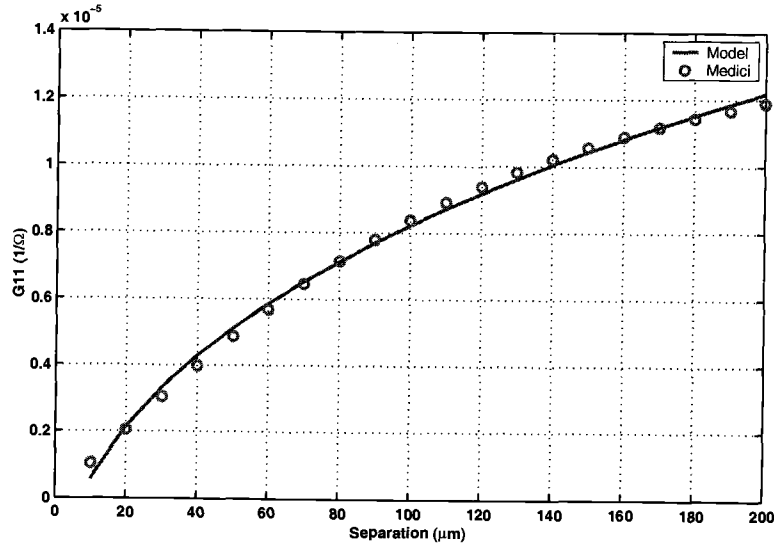


Figure 3.6. Comparison of the model for conductance G_{11} with MEDICI simulations for a lightly doped substrate without a buried layer.

3.4. Analysis of Lightly Doped Substrate Without a Buried Layer

The dependence of G_{11} and G_{12} on the separation of the contacts in a lightly doped substrate without a buried layer (Fig. 3.1) is now examined. The plots of the variation of G_{11} and G_{12} with separation are shown in Figs. 3.6 and 3.7 respectively. The relationship of G_{11} with separation x can be expressed as:

$$G_{11} = \alpha + \beta x + \epsilon \sqrt{x} \quad (3.3)$$

where α , β and ϵ are process dependent parameters. The values of these parameters for the lightly doped substrate without a buried layer considered here are given by:

$$\alpha = -3.4 \times 10^{-8} \frac{1}{\Omega} \quad \beta = -1.48 \times 10^{-2} \frac{1}{\Omega m} \quad \epsilon = 1.314 \times 10^{-3} \frac{1}{\Omega \sqrt{m}}$$

The plot in Fig. 3.6 shows a good agreement between the model in (3.3) and the simulated values extracted from MEDICI. The G_{11} model derived in (3.3) is valid only for separations greater than $10\mu m$. Figure 3.7 shows that the variation

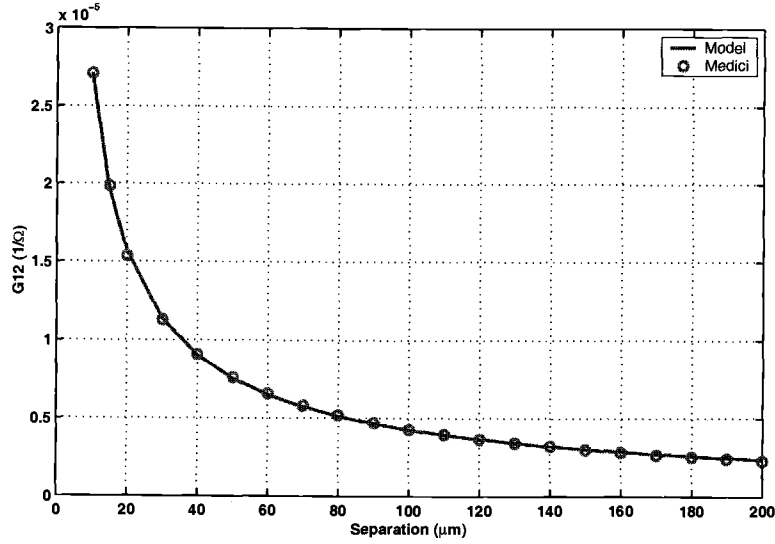


Figure 3.7. Comparison of the model for conductance G_{12} with MEDICI simulations for a lightly doped substrate without a buried layer.

of G_{12} with separation decreases as the separation between the contacts increases.

This behavior can be expressed as:

$$G_{12} = \frac{1}{a + bx} \quad (3.4)$$

The values of a and b are constant for a particular process and for this process are given by:

$$a = 1.41 \times 10^4 \, \Omega \quad b = 2.35 \times 10^9 \, \frac{\Omega}{m}$$

The values of R_{11} and R_{12} obtained for different values of separation between the source and the sensor are calculated using (3.3) and (3.4). These are then compared with the resistance values extracted from MEDICI for a lightly doped substrate without a buried layer. These comparisons are shown in Table 3.3.

Table 3.3. A comparison of the simulated results with the model used to predict the resistance values of the substrate network for a lightly doped substrate without the buried layer.

Separation (μm)	R_{11} (K Ω)		R_{12} (K Ω)		<i>RelativeError</i>	
	Model	Sim.	Model	Sim.	R_{11}	R_{12}
10	1748	1574	37.7	36.8	9.8%	2.2%
20	466	487	49.5	50.3	4.5%	1.6%
30	302	319	61.3	65.2	5.3%	6.1%
40	233	241.8	84.8	88.5	3.3%	4.2%
50	195	205	108.4	110.4	4.8%	1.7%
70	170	175	155	152	2.85%	2.3%
80	153	155	179	172.4	1.29%	3.9%
90	140	139	202	192.5	0.71%	5.2%

Table 3.3 shows that the values of R_{11} and R_{12} obtained from MEDICI simulations are in agreement with the model given in (3.3) and (3.4). A comparison of the data in Table 3.3 shows that the worst case error for the vertical resistance R_{11}

when using the model is about 9.9% for a separation of $10\mu m$ and the worst case error for the cross coupling resistance R_{12} is 5.2% for a separation of $90\mu m$.

3.5. Z-Parameter Based Model

The resistance model discussed so far is simple, intuitive and accurate. However, it is not applicable when multiple contacts are involved. This is because the additional contacts change the entire resistive network. This is illustrated as follows. Consider a two contact problem with $5\mu m \times 5\mu m$ size contacts at a separation of $x = 30\mu m$. The simulated resistance values are shown in Fig. 3.8 (a). When another contact is added to this configuration at a separation of $30\mu m$, the resistance network changes from the two contact case as shown in Fig. 3.8 (b).

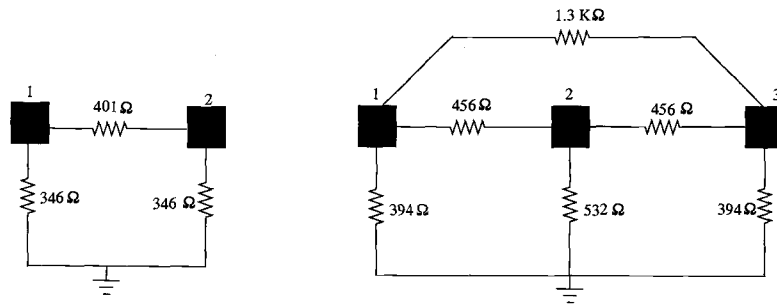


Figure 3.8. Resistance network for (a) two identical contacts (b) three identical contacts.

If the two-port resistive model is extended to a multiple contact case, the resistance values should remain constant which results in incorrect values. In order to develop a generalized model, a representation has to be used that includes the

effect of nearby contacts. A macromodel based on open-circuit parameters or Z-parameters addresses this problem [10]. The open circuit parameters are defined as follows:

$$\begin{bmatrix} v_i \\ v_j \end{bmatrix} = \begin{bmatrix} z_{ii} & z_{ij} \\ z_{ji} & z_{jj} \end{bmatrix} \begin{bmatrix} i_i \\ i_j \end{bmatrix} \quad (3.5)$$

3.6. Extending the Model to Multiple Contacts

As described above, the model for multiple contacts is based on Z-parameters. The following process as described in [10] is used to generate the resistance matrix for multiple contacts:

1. The 2-port Z-parameters are calculated based on the contact size and separation information. Considering two contacts i and j , the Z-matrix is given as:

$$Z = \begin{bmatrix} z_{ii} & z_{ij} \\ z_{ji} & z_{jj} \end{bmatrix} \quad (3.6)$$

2. 2×2 Z-parameter matrices are generated for each contact pair. Then the $N \times N$ Z-matrix is constructed by combining the 2-port Z-parameter matrices into a single Z-parameter matrix.

$$Z = \begin{bmatrix} \cdot & \cdot & \cdot & \cdot & \cdot & \cdot & \cdot \\ \cdot & z_{ii} & \cdot & \cdot & z_{ij} & \cdot & \cdot \\ \cdot & \cdot & \cdot & \cdot & \cdot & \cdot & \cdot \\ \cdot & \cdot & \cdot & \cdot & \cdot & \cdot & \cdot \\ \cdot & \cdot & \cdot & \cdot & \cdot & \cdot & \cdot \\ \cdot & z_{ji} & \cdot & \cdot & z_{jj} & \cdot & \cdot \\ \cdot & \cdot & \cdot & \cdot & \cdot & \cdot & \cdot \\ \cdot & \cdot & \cdot & \cdot & \cdot & \cdot & \cdot \end{bmatrix} \quad (3.7)$$

The $N \times N$ Z-parameter matrix constructed from the 2-port parameters is shown in (3.7)

3. The resistance values can be extracted from the Y-matrix which is obtained by inverting the $N \times N$ Z-matrix.

The dependence of Z_{11} on contact size in lightly doped substrates is examined here. For a two contact case, the width of the contact is changed from $0.5\mu m$ to $80\mu m$ and Z_{11} values are obtained for processes with and without a buried layer from MEDICI simulations. The variation of Z_{11} with contact width is shown in Figs. 3.9 and 3.11, for the two cases.

From Fig. 3.10, it can be seen that there is a linear relationship between $\frac{1}{Z_{11}}$ and the contact width. Therefore, Z_{11} can be expressed as

$$Z_{11} = \frac{1}{\alpha + \beta W} \quad (3.8)$$

where α and β extracted from curve-fitting are:

$$\alpha = 9.395 \times 10^{-6} \frac{1}{\Omega} \quad \beta = 4.338 \times 10^{-2} \frac{1}{\Omega m}$$

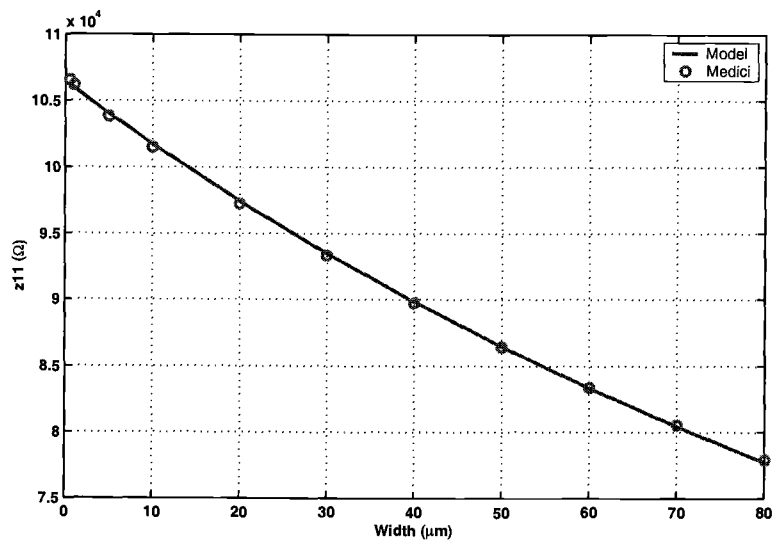


Figure 3.9. Z_{11} versus contact width in a lightly doped substrate with a buried layer.

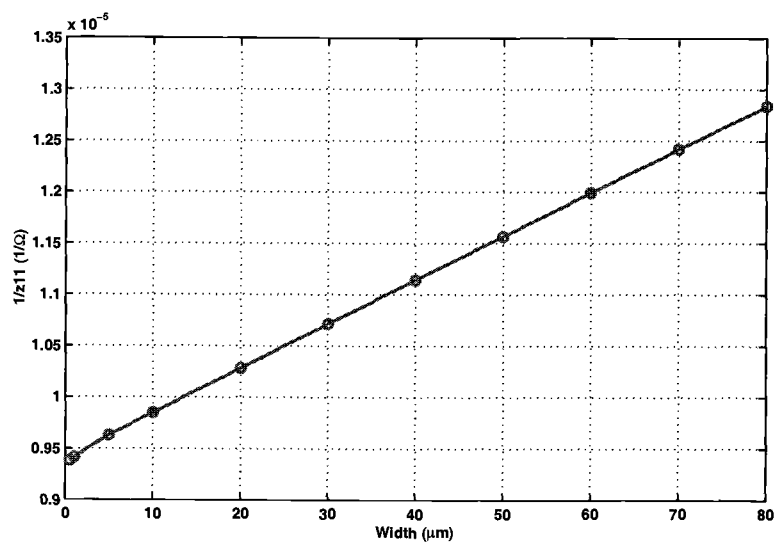


Figure 3.10. $\frac{1}{Z_{11}}$ varies linearly with contact width in a lightly doped substrate with a buried layer.

An examination of Fig. 3.9 shows that Z_{11} does not vary much with contact width. Since the heavily doped P+ implant layer has a much lower resistance than the bulk, current from the injector spreads on the surface before flowing into the backplane. This spreading of current around the contact makes the effective width of the contact appear greater than the actual width. It is seen from Fig. 3.9 that the model in (3.8) predicts the simulated value of Z_{11} accurately. In a lightly doped substrate without

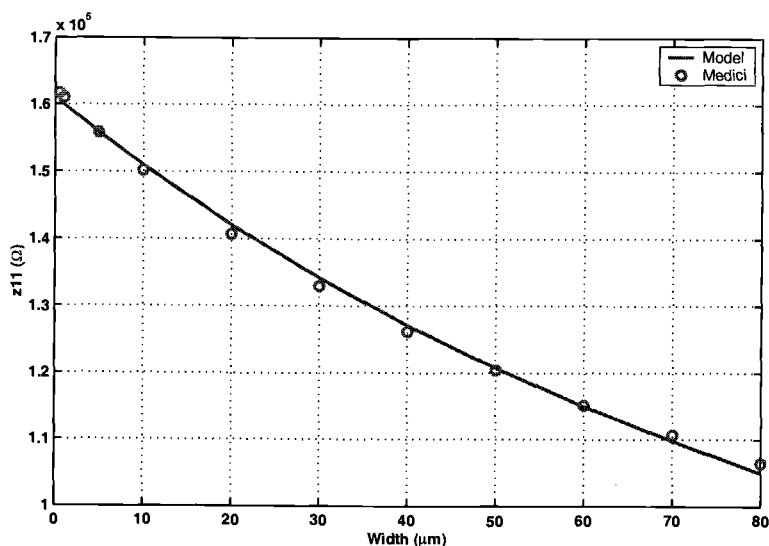


Figure 3.11. Z_{11} versus contact width in a lightly doped substrate without a buried layer.

a buried layer, as well, $1/Z_{11}$ shows a linear variation with the contact width as shown in Fig. 3.11 and α and β extracted for this process are given by:

$$\alpha = 6.210 \times 10^{-6} \frac{1}{\Omega} \quad \beta = 4.148 \times 10^{-2} \frac{1}{\Omega m}$$

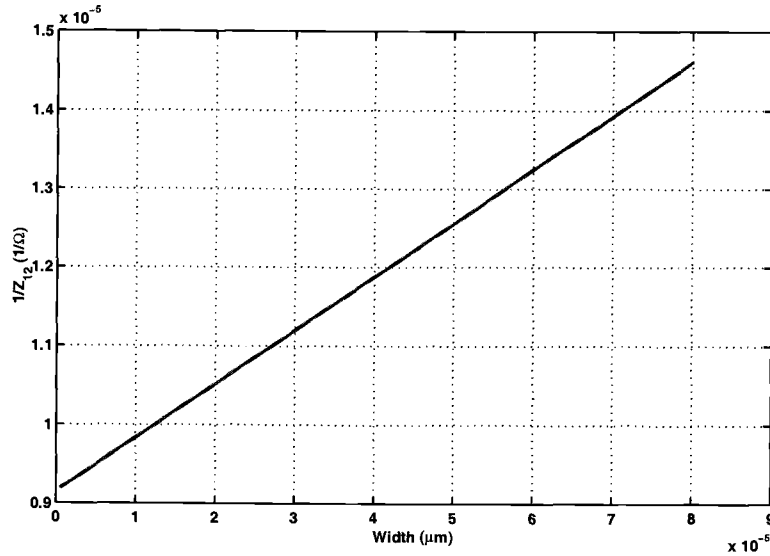


Figure 3.12. $\frac{1}{Z_{12}}$ versus contact width in a lightly doped substrate without a buried layer.

The dependence of Z_{12} on contact width for a lightly doped substrate with and without a buried layer is examined in a similar manner by varying the contact width from $0.5\mu m$ to $80\mu m$. From Fig. 3.12 it is seen that $\frac{1}{Z_{12}}$ varies linearly with contact width in a lightly doped substrate which can be expressed as:

$$Z_{12} = \frac{1}{A + BW} \quad (3.9)$$

Figure 3.13 shows the model of Z_{12} that matches the simulated values accurately.

A summary of all the equations and the corresponding parameters derived for the two processes are shown in Table 3.4.

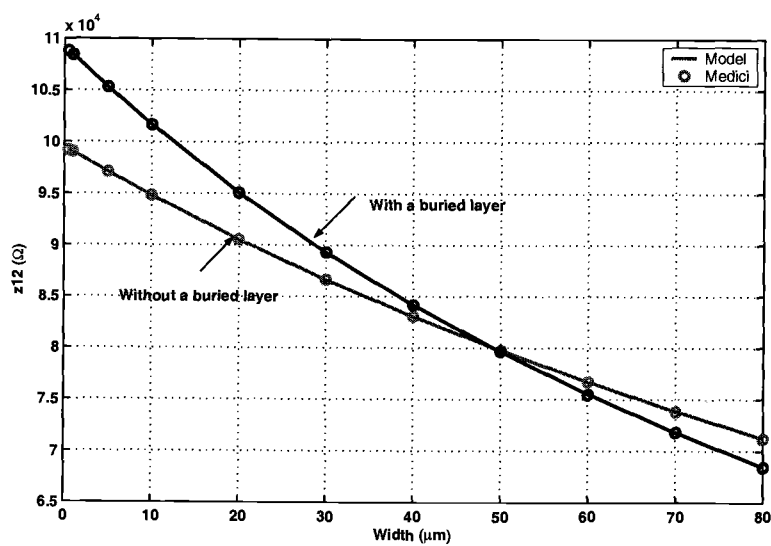


Figure 3.13. Z_{12} versus contact width in a lightly doped substrate with and without a buried layer.

Table 3.4. Summary of equations and parameters extracted for the two lightly doped processes.

Conductances	Equation	Parameters for lightly doped substrate with buried layer	Parameters for lightly doped substrate without buried layer
G_{11}	$\alpha + \beta x + \varepsilon \sqrt{x}$	$\alpha = -1.9 \times 10^{-6} \frac{1}{\Omega}$ $\beta = -3.21 \times 10^{-2} \frac{1}{\Omega m}$ $\varepsilon = 1.02 \times 10^{-3} \frac{1}{\Omega \sqrt{m}}$	$\alpha = -3.4 \times 10^{-6} \frac{1}{\Omega}$ $\beta = -1.48 \times 10^{-2} \frac{1}{\Omega m}$ $\varepsilon = 1.31 \times 10^{-3} \frac{1}{\Omega \sqrt{m}}$
G_{12}	$\frac{1}{a + bx}$	$a = 2.56 \times 10^{-3} \frac{\Omega}{1}$ $b = 2.55 \times 10^{-8} \frac{1}{\Omega}$	$a = 1.41 \times 10^{-4} \frac{\Omega}{1}$ $b = 2.35 \times 10^{-9} \frac{1}{\Omega}$
Z_{11}	$\frac{1}{\alpha + \beta W}$	$\alpha = 9.395 \times 10^{-6} \frac{1}{\Omega}$ $\beta = 2.55 \times 10^{-2} \frac{1}{\Omega m}$	$\alpha = 6.21 \times 10^{-6} \frac{1}{\Omega}$ $\beta = 4.148 \times 10^{-2} \frac{1}{\Omega m}$
Z_{12}	$\frac{1}{A + BW}$	$A = 1 \times 10^{-5} \frac{1}{\Omega}$ $B = 4.98 \times 10^{-2} \frac{1}{\Omega m}$	$A = 9.15 \times 10^{-6} \frac{1}{\Omega}$ $B = 6.81 \times 10^{-2} \frac{1}{\Omega m}$

4. EXTENSION OF THE MACROMODEL TO THE THIRD DIMENSION

4.1. Introduction

MEDICI is a 2D simulator that allows modeling the effect of separation between contacts and the variation of the width of the contact. The length of the contact, the dimension perpendicular to the 2D structure shown in Fig. 4.1 cannot be varied using the 2D simulator MEDICI. In an actual problem, the contacts can be of any shape and size and with different lengths. In order to develop a macromodel

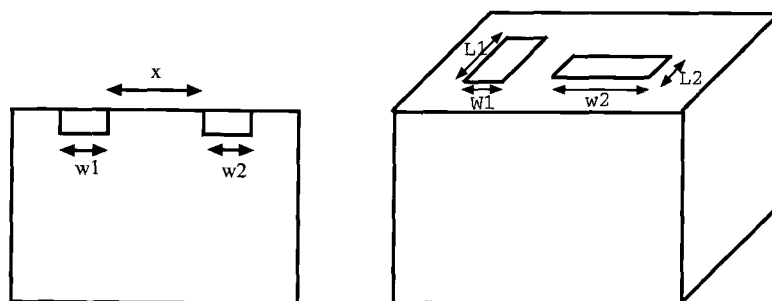


Figure 4.1. Two-dimensional and three-dimensional views of substrate contacts.

scalable with separation as well as contact dimensions, the 3D simulators Cadence-SCA [15] and EPIC [16] were used. SCA uses an integral equation solver (IES3) based on a Poisson's equation based field solver. IES3 uses an efficient Green's function and matrix compression to generate the resistive substrate network. The key information provided to SCA are the process parameters such as the substrate doping profile and the layer thicknesses as well as contact dimensions and separations. These 3D simulations were verified using EPIC, another 3D simulator, that extracts

the substrate resistances and capacitances using the Green's function method. The extra information to be provided to EPIC is the die area.

4.2. 3D Model of Lightly Doped Substrate Without a Buried Layer

An analysis of the results obtained from simulations shows that Z_{11} remains constant as the contact separation x is increased as shown in Fig. 4.2. Next, the dependence of Z_{11} on nearby contacts is examined. Figure 4.3 shows the different cases considered. For a single contact of $10\mu m \times 10\mu m$, Z_{11} as obtained from SCA is $236\ \Omega$. When another contact of the same dimension is placed at a separation of $5\mu m$, the value of Z_{11} is $234\ \Omega$. In the third case, with two contacts on each side, Z_{11} is $233.5\ \Omega$. From these results it can be concluded that Z_{11} does not vary significantly due to the presence of nearby contacts.

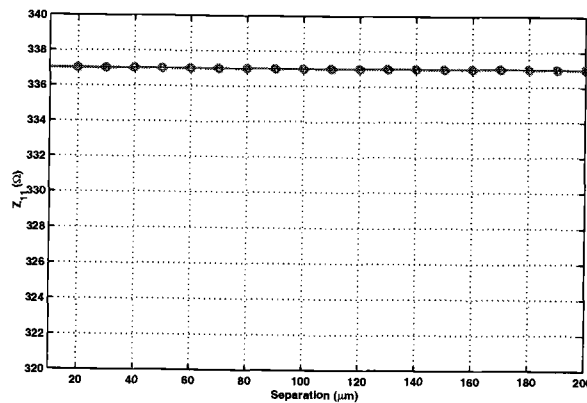


Figure 4.2. Z_{11} as a function of separation.



Figure 4.3. Effect of nearby contacts on Z_{11} .

The next step in developing the macromodel is to characterize the effect of the contact size on Z_{11} . From the data extracted from SCA simulations for different contact sizes, Z_{11} can be expressed as a function of the contact area and perimeter as shown below:

$$Z_{11} = \frac{1}{A + B \text{Area} + C \text{Perimeter}} \quad (4.1)$$

where A , B and C are process parameters and are given by:

$$A = 3.98 \times 10^{-4} \quad \frac{1}{\Omega} \quad B = 23.31 \quad \frac{1}{\Omega m^2} \quad C = 9.134 \quad \frac{1}{\Omega m}$$

Figure 4.4 compares the Z_{11} value obtained using the model in (4.1) with the simulated data extracted from SCA simulations. There is a good agreement between the model and simulations with the maximum percentage error being less than 7%.

In order to obtain a general macromodel for Z_{12} , the effect of contact sizes and separations on Z_{12} is analyzed. The dependence of Z_{12} on separation, x , between the contacts is examined first. The simulated data is shown in Fig. 4.5. It is observed from this plot that for small separations, $\log(Z_{12})$ has a large variation. For large separations, $\log(Z_{12})$ varies linearly with separation. This behavior can be modeled as:

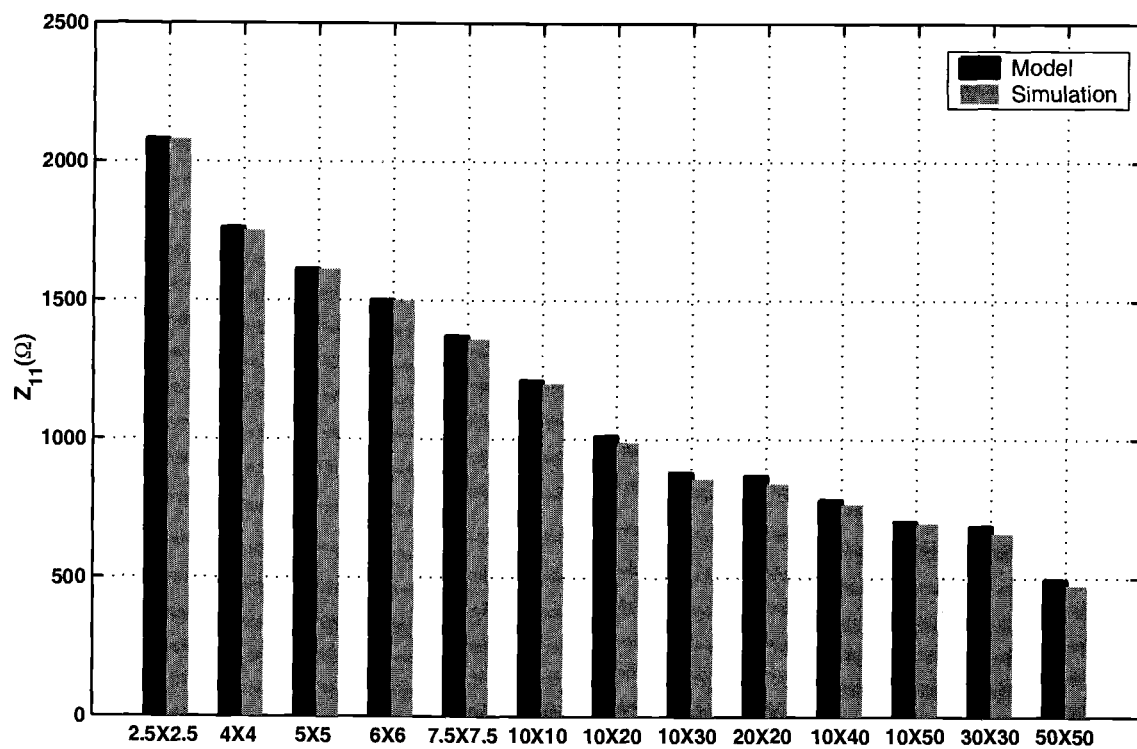


Figure 4.4. The Z_{11} model is in good agreement with SCA simulations.

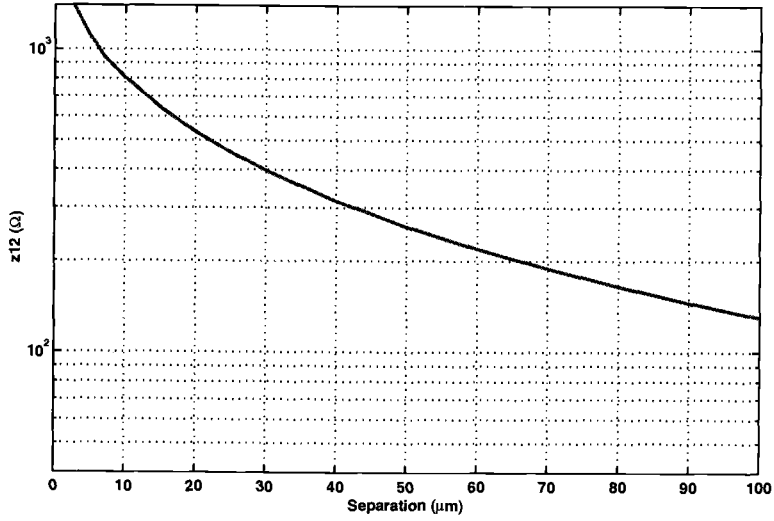


Figure 4.5. Z_{12} versus separation.

$$Z_{12} = \frac{\alpha e^{-\beta x}}{\epsilon + \sqrt{x}} \quad (4.2)$$

where α , β , and ϵ are process parameters obtained from simulations or measurements. The logarithm of (4.2) is given as:

$$\log(Z_{12}) = \log \alpha - \log(\epsilon + \sqrt{x}) - \beta x \quad (4.3)$$

For large x ,

$$\frac{\log x}{x} \ll 1 \quad (4.4)$$

and the $\log x$ term is negligible compared to x , and $\log \alpha$ is a constant. Thus, the logarithm of Z_{12} at large separations has a linear dependence on x . According to

the model, in the limiting cases

$$x \rightarrow \infty, Z_{12} \rightarrow 0 \quad (4.5)$$

$$x \rightarrow 0, Z_{12} \rightarrow \frac{\alpha}{\epsilon} \quad (4.6)$$

This is an expected physical behavior for Z_{12} and can be explained in terms of the resistances R_{11} and R_{12} . For the resistance network shown in Fig. 2.1, the open circuit parameter Z_{12} can be written as:

$$Z_{12} = \frac{R_{11}R_{22}}{R_{11} + R_{12} + R_{22}} \quad (4.7)$$

As

$$x \rightarrow \infty, R_{12} \rightarrow \infty \quad Z_{12|_{R_{12} \rightarrow \infty}} = 0 \quad (4.8)$$

As

$$x \rightarrow 0, R_{12} \rightarrow 0 \quad Z_{12|_{R_{12} \rightarrow 0}} = \frac{R_{11}R_{22}}{R_{11} + R_{22}} \quad (4.9)$$

which is a constant value given by the ratio of α and ϵ in the model.

Figure 4.6 shows that the model for Z_{12} given in (4.2) predicts the Z_{12} value extracted from simulations accurately. In order to incorporate the effect of contact size on Z_{12} , the relationships of α , β and ϵ on contact dimension have to be determined. From simulations performed by varying the contact area and perimeter, it is observed that β is independent of contact sizes and is a constant value for a given process. For a lightly doped substrate without a buried layer, the value of β is given by $6.66 \times 10^3 \frac{1}{m}$.

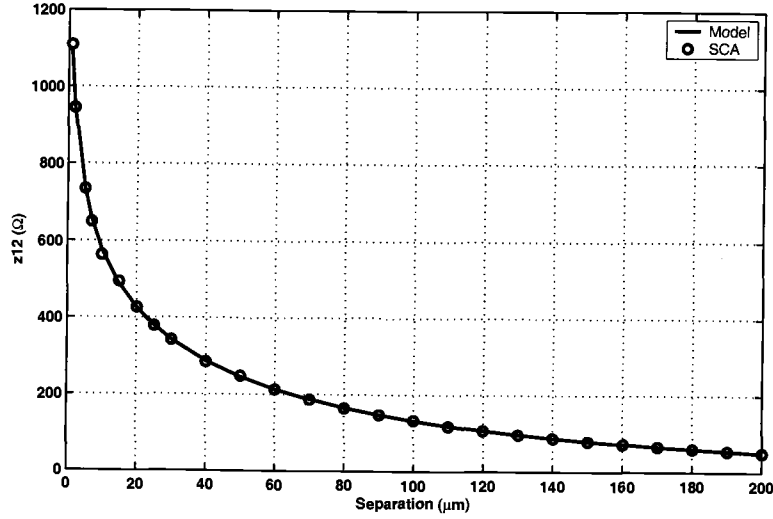


Figure 4.6. Z_{12} versus separation for $1\mu m \times 1\mu m$ contacts.

A similar analysis was also performed for the coefficients α and ϵ . The dependence of α and ϵ on contact dimensions are shown in Figs. 4.7 and 4.8. It can be seen from the plots that both α and ϵ vary linearly with the perimeter of the merged contacts.

Therefore,

$$\alpha = A + B(P_{merged}) \quad (4.10)$$

$$\epsilon = C + D(P_{merged}) \quad (4.11)$$

where P_{merged} is the perimeter when the two contacts are merged together.

From this analysis, it can be concluded that the macromodel in (4.2) is scalable with contact size as well as separation, x , once the constants for a particular

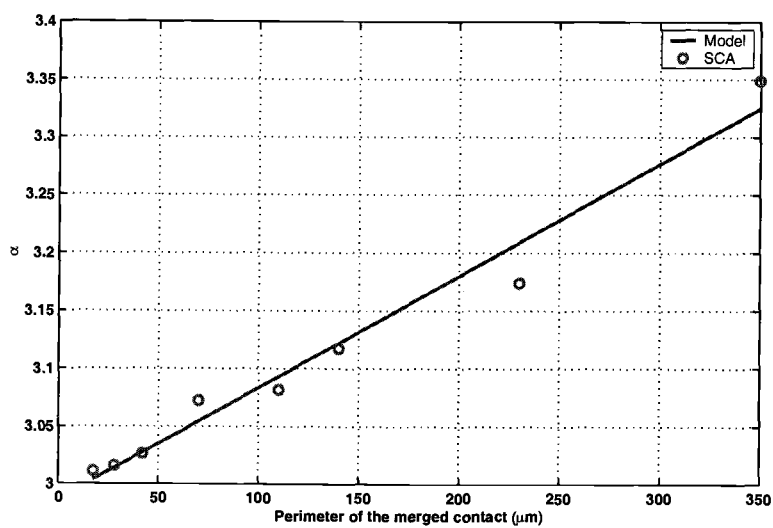


Figure 4.7. α as a function of the perimeter of the merged contacts.

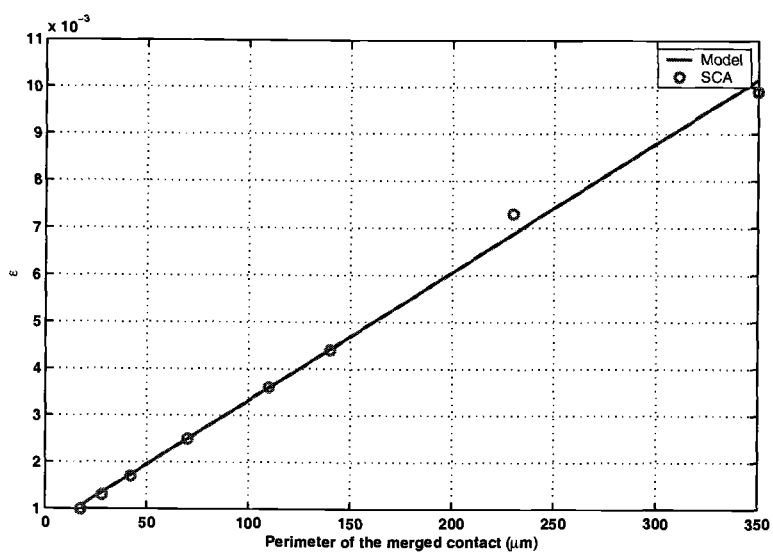


Figure 4.8. ϵ as a function of the perimeter of the merged contacts.

process are known. These constants can be extracted by curve-fitting simulated or measured data.

Model for Contacts with Different Sizes

The model in (4.2) was developed considering identical square or rectangular contacts. However, in practice, the contacts may be of different sizes. This introduces the effect of another dimension or the relative position of the contacts when one contact is smaller than the other. This effect is incorporated into the macromodel next. Shown in Fig. 4.9 is an example of two non-identical contacts when contact A is bigger than contact B. In this case, B can be moved along the x direction as well as the y direction.

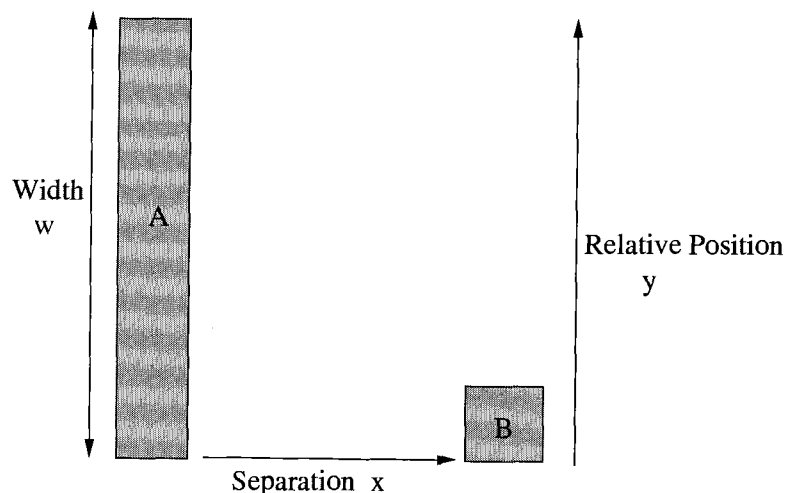


Figure 4.9. An example of two contacts with different sizes.

When the relative position y is zero, the bottom edges of the two contacts are aligned with each other. When y is zero and the smaller contact B only moves along the x -axis, the variation of Z_{12} with separation x is shown in Fig. 4.10. It is seen that Z_{12} in Fig. 4.10 has the same behavior as Z_{12} for identical contacts. So, (4.2) can be used to predict the effect of separation x on Z_{12} between contacts with different sizes. In order to characterize the effect of y on Z_{12} , the separation between

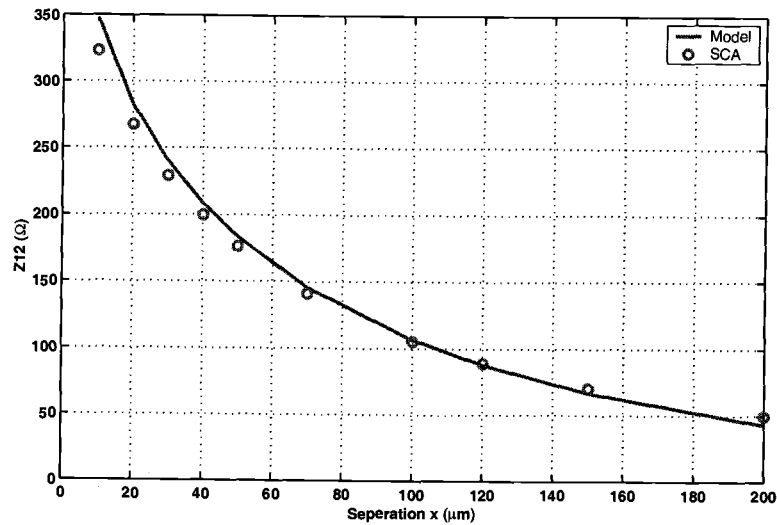


Figure 4.10. Simulations and model for Z_{12} show a good agreement for non-identical contacts when $y=0$.

the contacts is fixed at x_0 . Figure 4.11 shows the variation of Z_{12} when the contact B is moved along the y direction at $x = x_0$. Z_{12} varies quadratically with y , similar to the heavily doped case [10] and can be modeled as:

$$Z_{12} = ay^2 + by + c \quad (4.12)$$

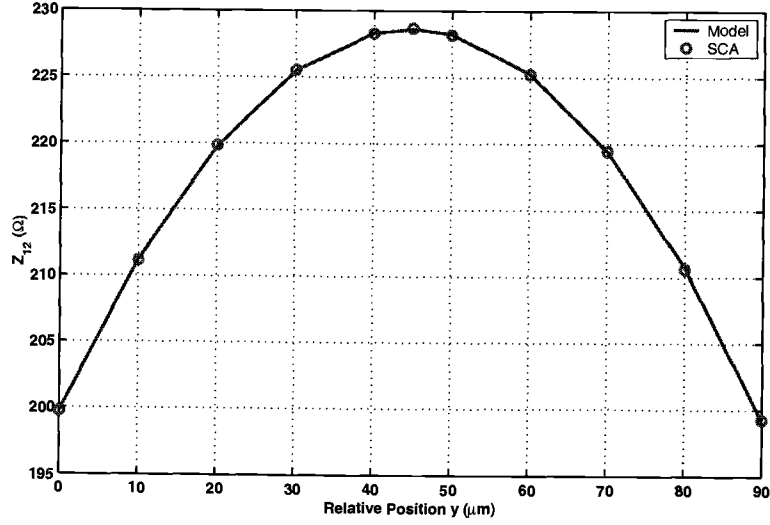


Figure 4.11. Simulations and model for Z_{12} show a good agreement for non-identical contacts when $x = 30\mu\text{m}$.

From Fig. 4.11, one can observe that the maximum value of Z_{12} occurs at the point when the centers of the two contacts are aligned with each other. From the quadratic expression (4.12), it is seen that

$$Z_{12}|_{y=0} = c \quad (4.13)$$

The symmetry of the Z_{12} curve with $w/2$ where w is the width of the contact A (Fig. 4.9) shows that the coefficients a and b are related to each other as a function

of the width w of the contact A. Therefore,

$$\frac{b}{2} = \frac{-aw}{2} \quad (4.14)$$

where w is the width of the larger contact. Modeling the dependence of Z_{12} on the relative position y requires an additional parameter a .

For simplicity, Z_{12} is expressed as

$$\frac{Z_{12}}{Z_{12}|_{y=0}} = (a_1 y^2 + b_1 y + 1) \quad (4.15)$$

where a_1 and b_1 are process dependent parameters.

From the data extracted from simulations for different values of x , it has been observed that a_1 shows a large variation with separation for small values of separation and starts flattening for larger values of separation x between the contacts (4.12). This behavior can be modeled as:

$$a_1 = K_1 + K_2 x + K_3 \sqrt{x} \quad (4.16)$$

where K_1 , K_2 and K_3 are process dependent parameters that are obtained from curve fitting measured or simulated data.

And,

$$\frac{b_1}{2} = \frac{-a_1 w}{2} \quad (4.17)$$

So, the generalized model of Z_{12} in a lightly doped substrate is given by

$$Z_{12} = (a_1 y^2 + b_1 y + 1) \left(\frac{\alpha e^{-\beta x}}{\epsilon + \sqrt{x}} \right) \quad (4.18)$$

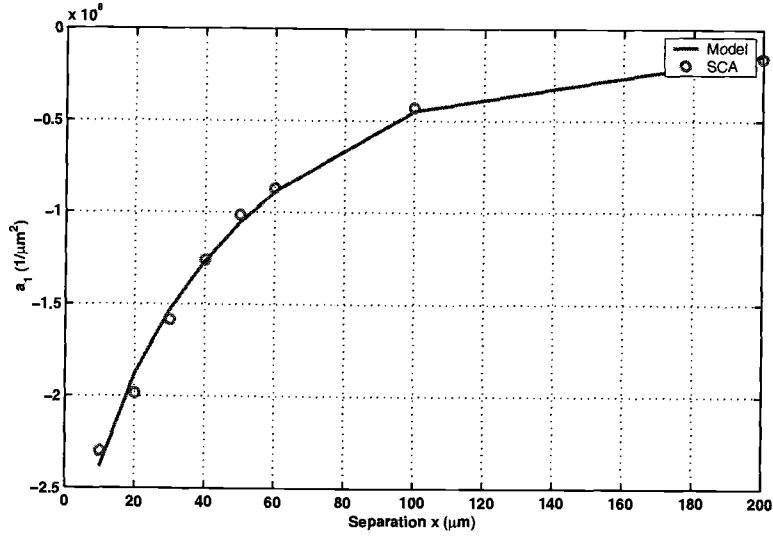


Figure 4.12. a_1 versus separation x .

where the parameters α and ϵ introduce the contact size dependence and a_1 is given in (4.16).

When the separation x and the relative position y are varied, Z_{12} is predicted using (4.18). Figure 4.13 shows that the model is in good agreement with simulated data.

4.3. 3D Model of Lightly Doped Substrate With a Buried Layer

The model for a lightly doped substrate with a buried layer is similar to that for the process without a buried layer. Using the same approach, first the dependence of Z_{11} on the various parameters is analyzed. Z_{11} is independent of the separation x between the contacts and does not vary with the presence of nearby

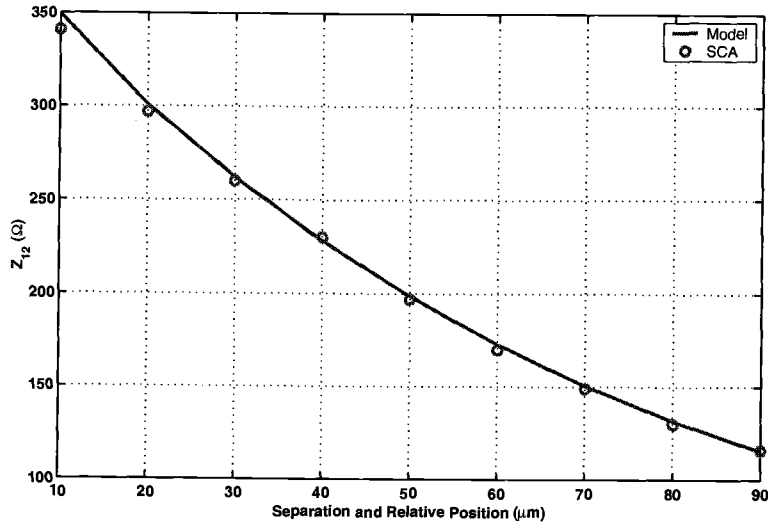


Figure 4.13. Comparison of the model for Z_{12} with SCA-3D simulations.

contacts. The only factors affecting the value of Z_{11} are the contact dimensions, therefore,

$$Z_{11} = \frac{1}{A + B \text{Area} + C \text{Perimeter}} \quad (4.19)$$

The coefficients depend on the process and for the lightly doped substrate with a buried layer are:

$$A = 2.539 \times 10^{-3} \frac{1}{\Omega}; \quad B = 23.3 \frac{1}{\Omega m^2} \quad C = 29.31 \frac{1}{\Omega m}$$

Figure 4.14 shows that the Z_{11} value obtained using the model is in good agreement with the value of Z_{11} extracted from simulations.

Z_{12} in a lightly doped substrate with a buried layer (Fig. 4.15) shows the same exponentially decreasing behavior as in a lightly doped substrate without a

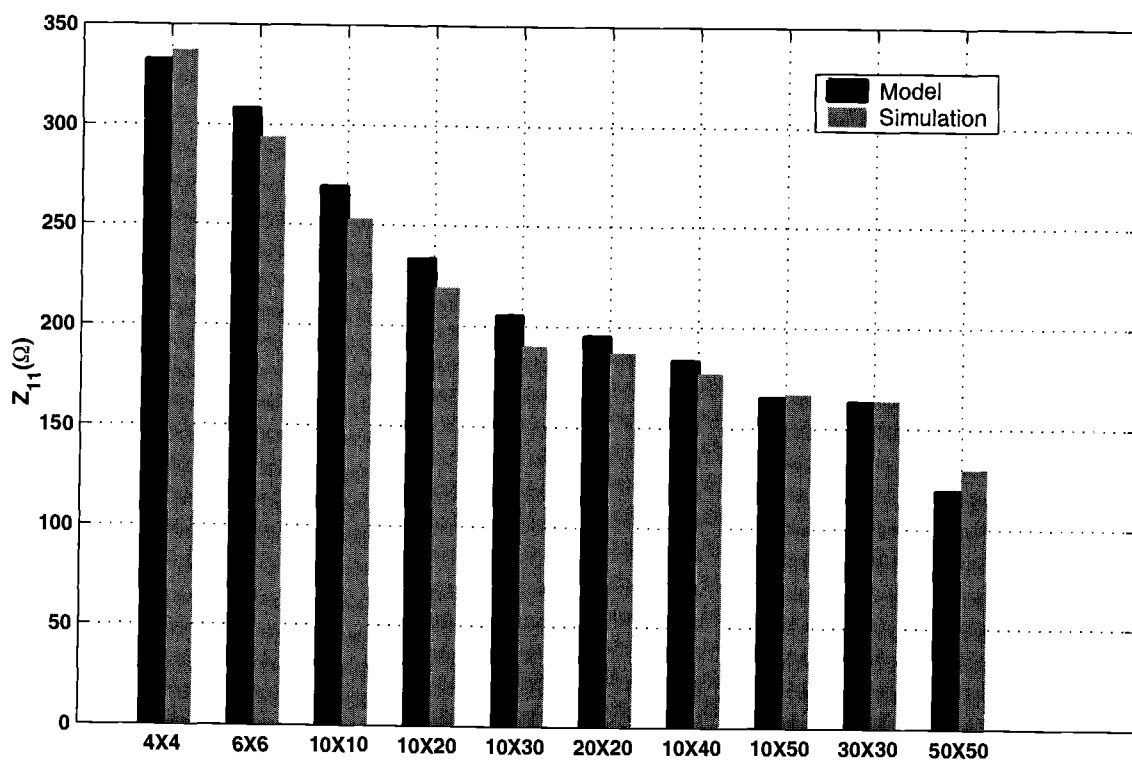


Figure 4.14. Simulations and the model for Z_{11} show good agreement.

buried layer. Thus a similar model can be used.

$$Z_{12} = \frac{\alpha e^{-\beta x}}{\epsilon + \sqrt{x}} \quad (4.20)$$

where α , β and ϵ are obtained by curve fitting data from simulations or measurements. β is found to be independent of contact dimensions and is equal to $3.43 \times 10^3 \frac{1}{m}$ for this substrate profile. The coefficients α and ϵ vary linearly with the perimeter of the merged contacts and are modeled as:

$$\alpha = A + B(P_{merged}) \quad (4.21)$$

$$\epsilon = C + D(P_{merged}) \quad (4.22)$$

where P_{merged} is the perimeter when the two contacts are merged together. The parameters, A, B, C and D are process dependent and for a lightly doped substrate with a buried layer are:

$$A = 1.179 \quad \Omega\sqrt{m} \quad B = 2.803 \times 10^3 \quad \frac{\Omega}{\sqrt{m}} \quad C = 3 \times 10^{-3} \quad \sqrt{m} \quad D = 43.41 \quad \frac{1}{\sqrt{m}}$$

Model for Contacts with Different Sizes

When the two contacts are not identical and one contact is larger than the other one (Fig. 4.9), the model has to be modified to take into account the relative position of the smaller contact with respect to the larger contact. Shown in Fig. 4.16 is the variation of Z_{12} with separation x when the bottom edges of the two contacts are aligned with each other. The model in (4.20) is a good predictor of the effect of separation x on Z_{12} . Figure 4.17 shows that at a fixed separation x_0 , Z_{12} has a quadratic dependence on the relative position y . This behavior can be modeled in the same way as for a lightly doped substrate without a buried layer given by:

$$Z_{12} = ay^2 + by + c \quad (4.23)$$

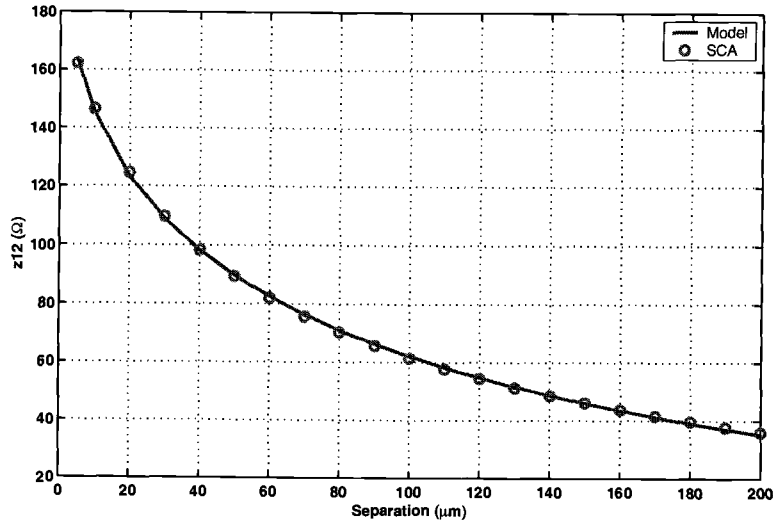


Figure 4.15. Simulations and the model for Z_{12} for a lightly doped substrate with a buried layer show good agreement.

When the separation x and the relative position y change at the same time, Z_{12} can be predicted using (4.24).

$$Z_{12} = (a_1 y^2 + b_1 y + 1) \left(\frac{\alpha e^{-\beta x}}{\epsilon + \sqrt{x}} \right) \quad (4.24)$$

Figure 4.18 shows that the expression in (4.24) and the simulation results show good agreement when both the separation x and the relative position y are varied.

4.4. Coupling due to Multiple Interacting Sides

Figure 4.19 shows an example of multiple interacting sides where the L-shaped contact surrounds the smaller contact on two sides. In order to calculate the effective Z_{12} between the two contacts, the complex structure is split into rectangular

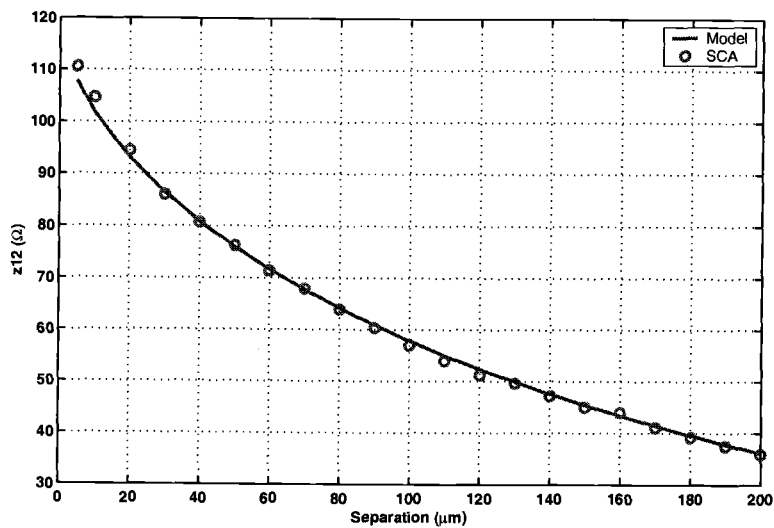


Figure 4.16. Simulations and the model for Z_{12} show good agreement for non-identical contacts for $y=0$.

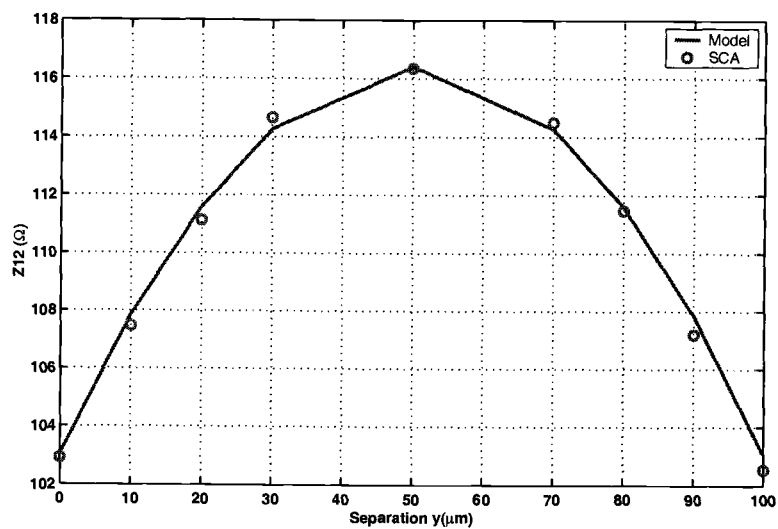


Figure 4.17. Simulations and model for Z_{12} show a good agreement for non-identical contacts for $x = 30\mu m$.

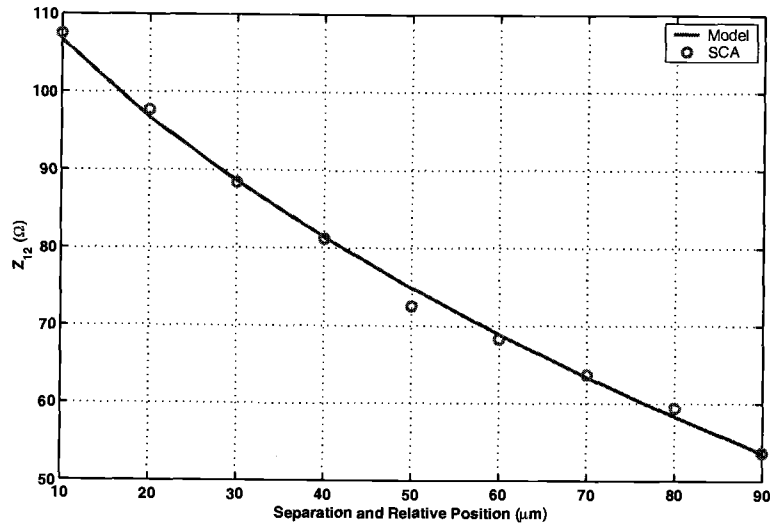


Figure 4.18. Simulations and the model for Z_{12} show good agreement for non-identical contacts.

contacts A and B. The coupling between each of these rectangular sections and the square contact is calculated separately. It has been found from simulations that the effective Z_{12} of the L-shaped structure is the average of the Z_{12} values obtained by dividing the complex structure. If Z_{12A} is the coupling between section A and the small square contact and Z_{12B} is the coupling between section B and the square contact, the overall Z_{12} of the geometry in Fig. 4.19 is given by:

$$Z_{12} = \frac{Z_{12A} + Z_{12B}}{2} \quad (4.25)$$

Z_{12A} and Z_{12B} can be readily calculated using the expression given in (4.24).

Shown in Fig. 4.20 is the variation of Z_{12} with relative position y for a particular separation x_0 . The curve A shows exponentially decaying behavior when only the coupling between contact A and the square contact are considered. The

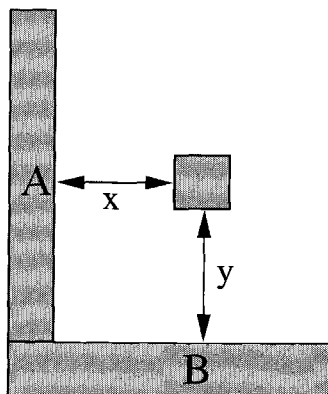


Figure 4.19. An L-shaped contact surrounding the square contact on two sides.

parabolic curve corresponds to the Z_{12} between contact B and the square contact since the relative position of the small contact is varied with respect to contact B in this case. Curve C is the effective Z_{12} due to the L-shaped contact which is the average of the first two curves.

From Fig. 4.20 it is seen that when the small contact is in position 1 (shown in Fig. 4.22), the maximum coupling is because of section A. When the small contact is in position 2, Z_{12} due to section B of the L-shaped contact is the major coupling component. At position 3, when the small square contact is equidistant from both the sections of the L-shaped contact, the coupling due to both sections is equal. This is the point of intersection of the A and B curves. Figure 4.21 shows that the model is in good agreement with simulations for different values of x .

Figure 4.23 shows the behavior of Z_{12} with variation in both separation x and the relative position y between the contacts. It can be concluded from Fig. 4.23 that the minimum coupling occurs when the square contact is aligned along the outer

edges of the two sections A and B which is an expected result. Shown in Fig. 4.24 are the constant contour lines of Z_{12} between the L-shaped structure and a square contact. As the small contact is moved along the curve from position 1 to 2 as illustrated in Fig. 4.22, Z_{12} remains constant.

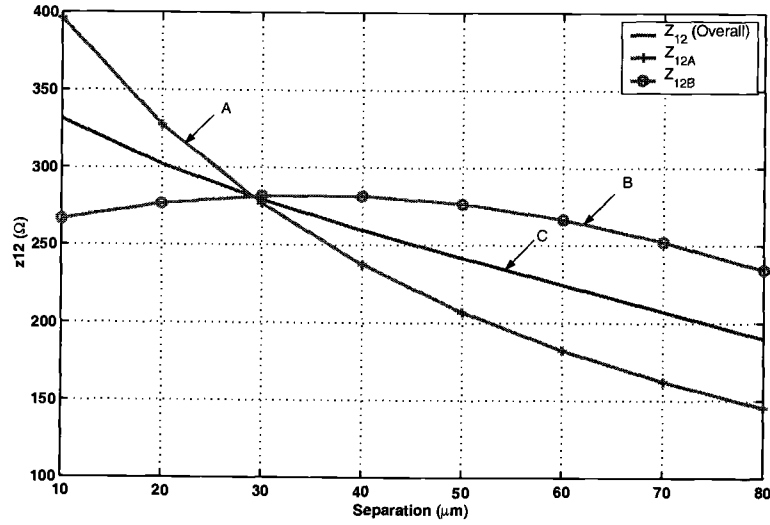


Figure 4.20. Z_{12} due to the two sections A and B of the L-shaped contact and overall Z_{12} (C).

The next case considered here is the interaction between a U-shaped contact (Fig. 4.25) and a square contact (Fig. 4.28). The model predicts that the effective Z_{12} is the average of Z_{12} obtained when the U-shaped contact is split into three rectangular sections. Figure 4.26 shows the comparison of the model with the simulated data for various values of x_0 . Figure 4.27 shows that the model predicts simulated data accurately for $x = 30\mu m$.

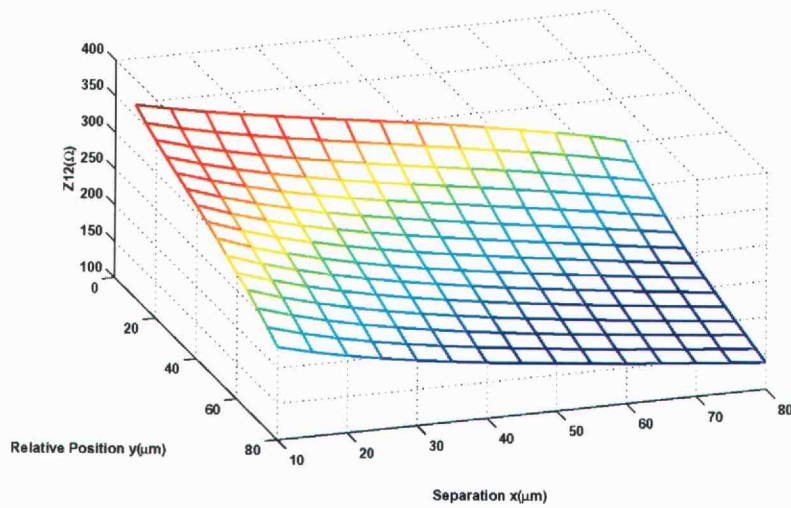


Figure 4.23. 3D plot showing the coupling between the two contacts in Fig. 4.19.

When the small contact is surrounded by a ring contact on all sides as shown in Fig. 4.28, it is seen that the Z_{12} is quadratically related to the separation x as well as the relative position y . From Fig. 4.29, it can be seen that the minimum value of Z_{12} occurs when the square contact is exactly in the middle of the ring contact. Figure 4.30 shows the comparison of the model with simulated data for $x_0 = 50\mu m$.

A summary of all the equations and the corresponding parameters for the two processes is shown in Table 4.1.

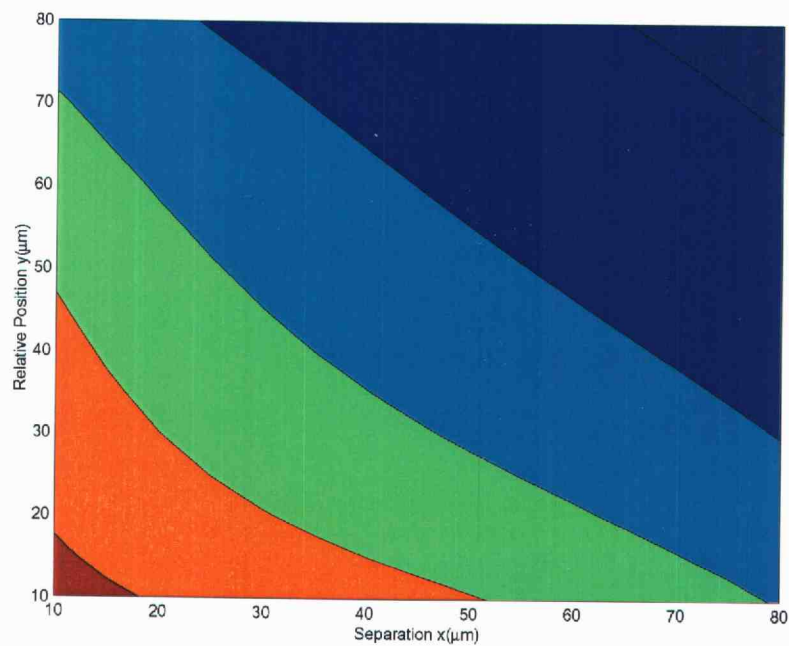


Figure 4.24. Constant Z_{12} contour lines for the L-shaped contact and the square contact case.

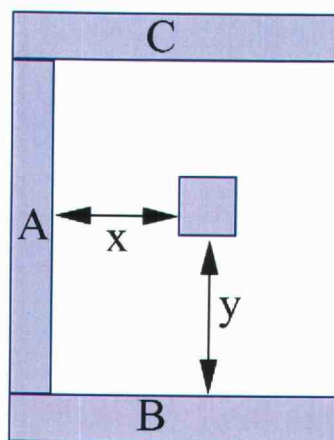


Figure 4.25. U-shaped contact surrounding the square contact on three sides.

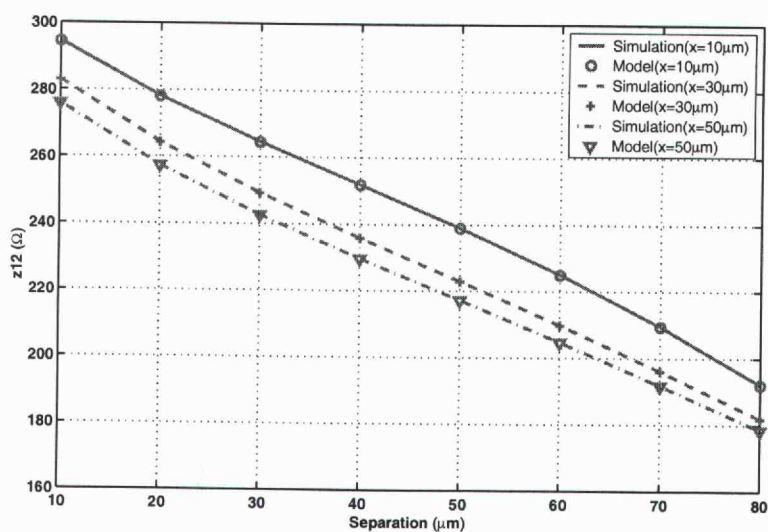


Figure 4.26. The model shows good agreement with simulated data for the geometry shown in Fig. 4.25.

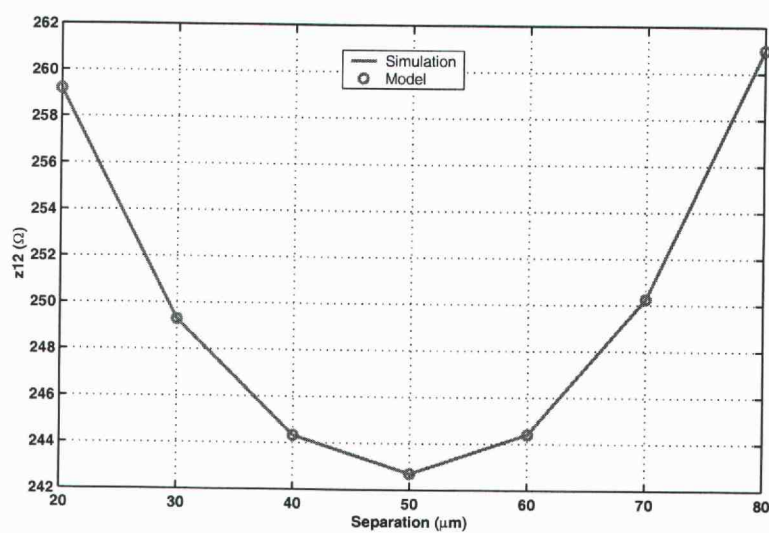


Figure 4.27. Simulated data versus model for Z_{12} for the structure shown in Fig. 4.25 for $x = 30\mu m$.

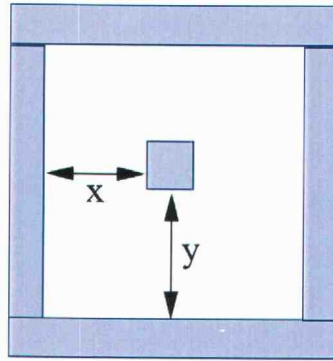


Figure 4.28. The square contact surrounded by another contact on all sides.

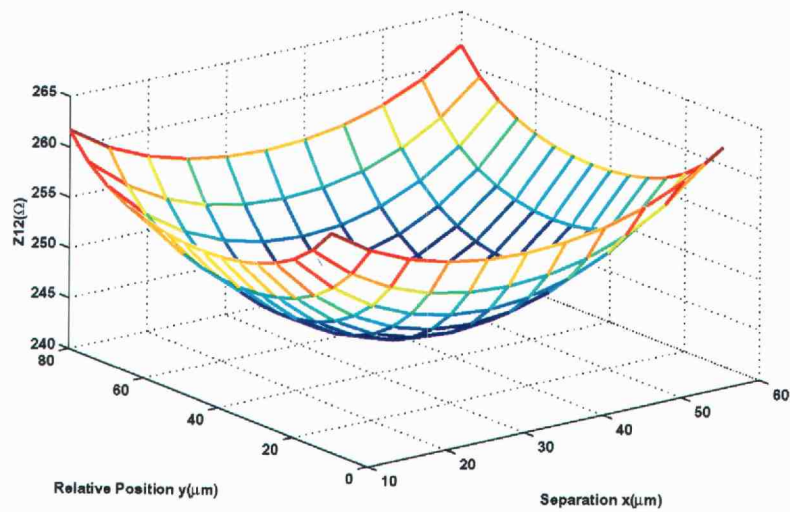


Figure 4.29. 3D plot of Z_{12} for the geometry shown in Fig. 4.28.

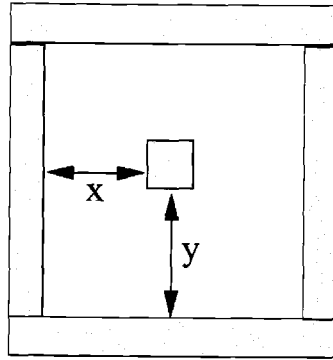


Figure 4.28. The square contact surrounded by another contact on all sides.

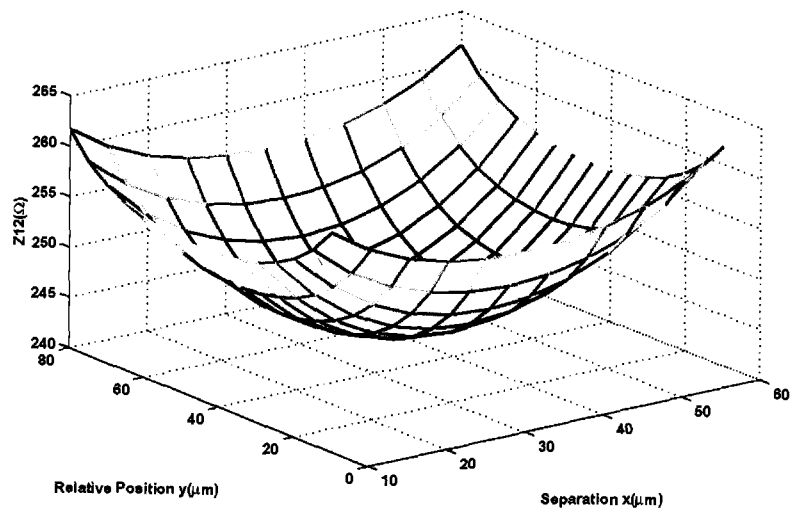


Figure 4.29. 3D plot of Z_{12} for the geometry shown in Fig. 4.28.

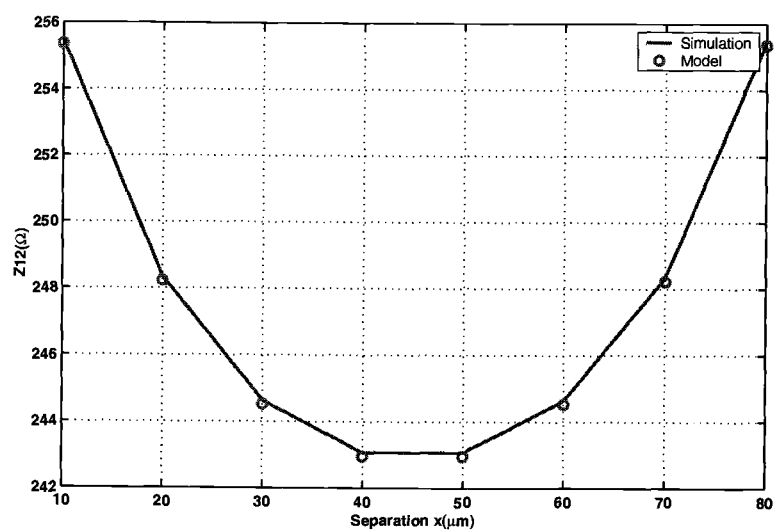


Figure 4.30. Model shows good agreement with simulations of Z_{12} for the geometry shown in Fig. 4.28 for $x_0 = 50 \mu m$.

Table 4.1. Summary of equations and parameters extracted for the two lightly doped processes.

Z-Parameters	Equation	Parameters for lightly doped substrate with buried layer	Parameters for lightly doped substrate without buried layer
Z_{11}	$\frac{1}{A + B\text{Area} + C\text{Perimeter}}$	$A = 3.98 \times 10^{-4} \frac{1}{\Omega}$ $B = 23.32 \frac{1}{\Omega m^2}$ $C = 9.134 \frac{1}{\Omega m}$	$A = 2.9 \times 10^{-4} \frac{1}{\Omega}$ $B = 23.3 \frac{1}{\Omega m^2}$ $C = 29.3 \frac{1}{\Omega m}$
Z_{12}	$\frac{\alpha e^{-\beta x}}{\varepsilon + \sqrt{x}} (a_1 y^2 + b_1 y + 1)$ <p>where, $\alpha = A + B(P_merged)$ $\varepsilon = C + D(P_merged)$ $\frac{b_1}{2} = \frac{a_1 w}{2}$ $a_1 = K_1 + K_2 x_a + K_3 \sqrt{x_a}$</p>	$\beta = 6.66 \times 10^3 \frac{1}{m}$ $A = 2.99 \frac{\Omega}{\sqrt{m}}$ $B = 2.0 \times 10^3 \frac{\Omega}{\sqrt{m}}$ $C = 5 \times 10^{-4} \frac{\Omega}{\sqrt{m}}$ $D = 27.93 \frac{\Omega}{\sqrt{m}}$ $K_1 = -1.6 \times 10^8 \frac{1}{m^2}$ $K_2 = 3.9 \times 10^{11} \frac{1}{m^3}$ $K_3 = 1.5 \times 10^{10} \frac{1}{m^{2.5}}$	$\beta = 3.37 \times 10^3 \frac{1}{m}$ $A = 1.18 \frac{\Omega}{\sqrt{m}}$ $B = 2.8 \times 10^3 \frac{\Omega}{\sqrt{m}}$ $C = 3 \times 10^{-3} \frac{\Omega}{\sqrt{m}}$ $D = 43.5 \frac{\Omega}{\sqrt{m}}$ $K_1 = -6.8 \times 10^7 \frac{1}{m^2}$ $K_2 = 8.8 \times 10^{10} \frac{1}{m^3}$ $K_3 = 5.42 \times 10^9 \frac{1}{m^{2.5}}$

5. MEASUREMENT RESULTS

A test chip was fabricated in a lightly doped substrate with a buried layer. The chip has several test structures as shown in Fig. 5.1 with P+ contacts of different sizes placed at different separations. A P+ guard ring which is grounded surrounds the entire setup. Test structures 1 and 2 are arrays of four contacts placed at different separations. Test structures 3, 4, and 5 are sets of contacts of the same size but at different separations.

The substrate resistances extracted from 2D (TMA-MEDICI) and 3D (SCA, EPIC) simulators are used in the setup shown in Fig. 5.2. R_{ij} denotes the resistances between the contacts i and j . R_{ig} is the resistance between the contact and ground. Applying a voltage of 1V at contact 1 and measuring the current flowing through the grounded contact 2 gives the value of resistance R_{1-2} . Similarly by grounding either of the other contacts and measuring the current through the contacts, R_{1-3} and R_{1-4} can be calculated.

Table 5.1 provides a comparison of the values of substrate resistances obtained using MEDICI, SCA and EPIC with the measured data. A comparison of the results in Table 5.1 shows that the results obtained from SCA and EPIC match the measured value accurately.

In order to validate the model, the same setup is evaluated using the model given earlier.

$$Z_{11} = \frac{1}{A + BArea + CPerimeter} \quad (5.1)$$

The contact size information is:

$$Area = 25\mu m^2 \quad Perimeter = 20\mu m$$

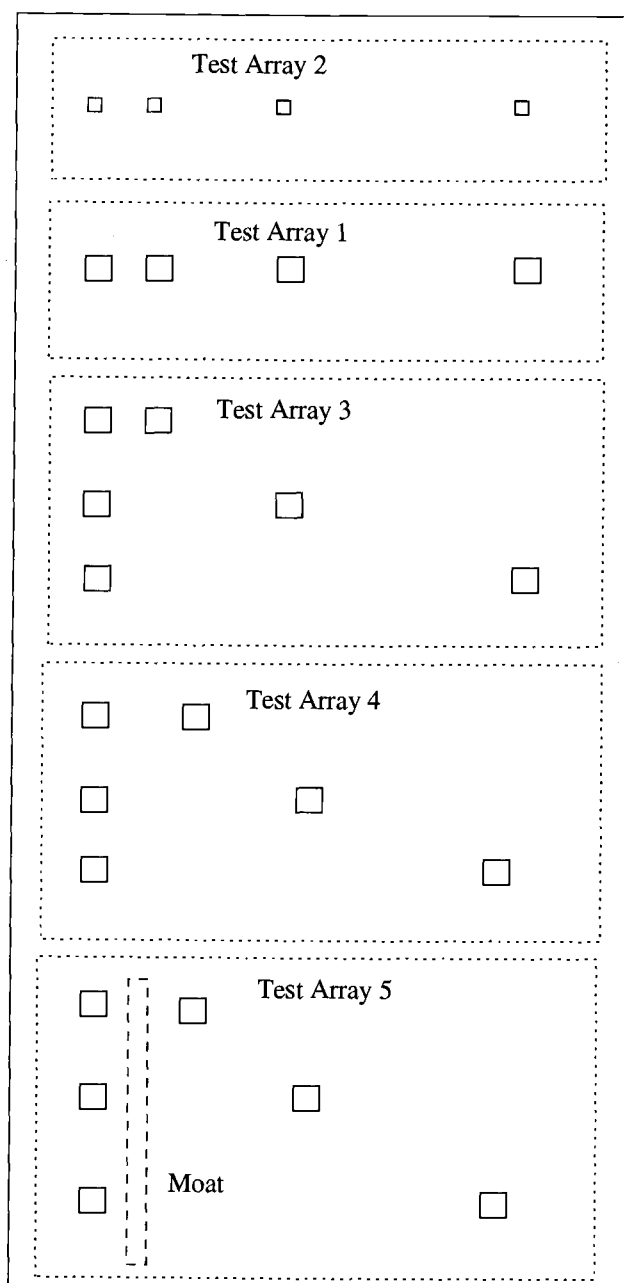


Figure 5.1. Layout of test structures.

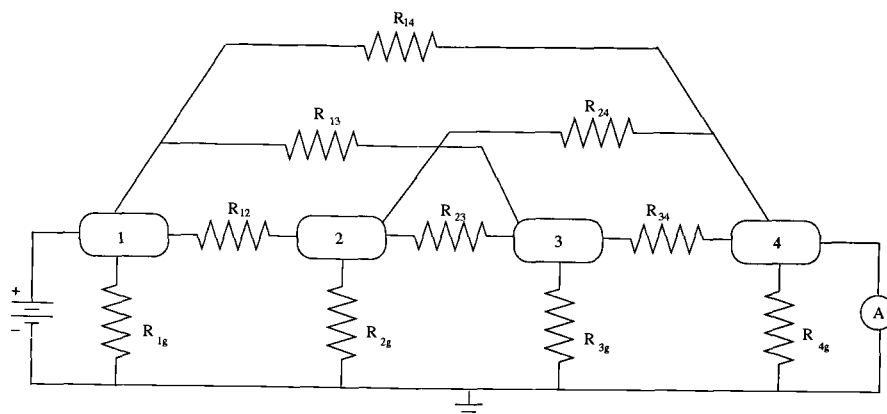


Figure 5.2. Simulation setup to evaluate R_{1-4} .

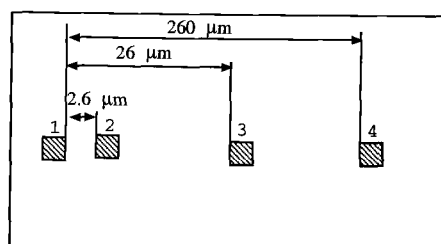


Figure 5.3. Array structure of $5\mu\text{m} \times 5\mu\text{m}$ contacts.

Table 5.1. Comparison of resistance values from 2D and 3D simulators with measured data for the test array shown in Fig. 5.3.

Resistances	Measured (Ω)	MEDICI ($K\Omega$)	SCA (Ω)	EPIC (Ω)	Model (Ω)
R_{1-2}	203.1	2.25	198	185	188
R_{1-3}	323.8	12.4	337	323	300
R_{1-4}	412.6	72.7	447	440	378

The coefficients A , B and C in (5.1) obtained from simulation are:

$$A = 2.539 \times 10^{-3} \frac{1}{\Omega} \quad B = 23.3 \frac{1}{\Omega m^2} \quad C = 29.3 \frac{1}{\Omega m}$$

Using the above information in (5.1), Z_{11} for a $5\mu m \times 5\mu m$ contact is equal to 319 Ω . Since the contacts are all of identical dimensions, to calculate Z_{12} , (5.2) is used.

$$Z_{12} = \frac{\alpha e^{-\beta x}}{\epsilon + \sqrt{x}} \quad (5.2)$$

Here, β is a constant and is equal to $3.43 \times 10^3 \frac{1}{m}$.

$$\alpha = K_{11} + K_{12}(P_{merged}) \quad (5.3)$$

$$\epsilon = K_{13} + K_{14}(P_{merged}) \quad (5.4)$$

where the coefficients K_{11} , K_{12} , K_{13} , K_{14} extracted from simulated data using a substrate with a buried layer are:

$$K_{11} = 1.179 \Omega \sqrt{m}, \quad K_{12} = 2.803 \times 10^3 \frac{\Omega}{\sqrt{m}}, \quad K_{13} = 3 \times 10^{-3} \sqrt{m}, \quad K_{14} = 43.39 \frac{1}{\sqrt{m}}$$

P_{merged} is the perimeter obtained when the two contacts are merged together as shown in Fig. 5.4. Z_{12} is calculated for various separations considering two contacts at a time and the four 2-port Z-matrices are constructed. The 4×4 Z-matrix is then formed from the 2-port Z-matrices and is given by:

$$Z = \begin{bmatrix} 319 & 211 & 122 & 26 \\ 211 & 319 & 137 & 27.5 \\ 122 & 137 & 319 & 30 \\ 26 & 27.5 & 30 & 319 \end{bmatrix} \quad (5.5)$$

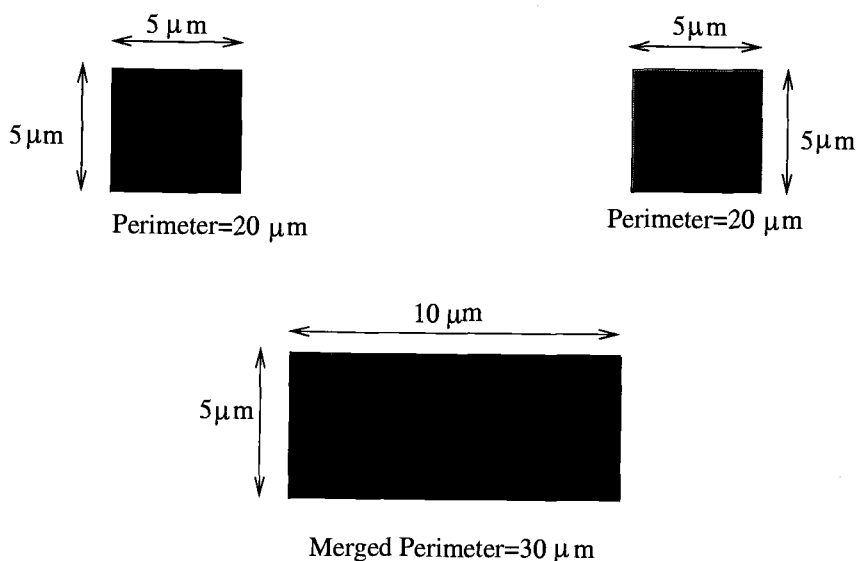


Figure 5.4. The two contacts are merged together to evaluate α and β .

The resistance matrix is then extracted from the Z-matrix and used in the simulation setup shown in Fig. 5.2. The resistance R_{1-2} is obtained by applying a voltage at contact 1 and grounding contact 2. Similarly other resistances are extracted. Figure 5.5 compares the measured value of R_{i-j} with that calculated using the model and shows a good agreement between the model and the measured resistances.

Test array 2 has a similar set of P+ contacts but of a different size. The simulation results are shown in Table 5.2. A comparison of the results in Table 5.2 shows that the results obtained from SCA match the measured values accurately. However, MEDICI results match the measured data only for R_{1-2} . For the other two cases, the resistance value obtained from MEDICI is several orders of magnitude greater than that compared to SCA. A comparison of the R_{1-2} value obtained from

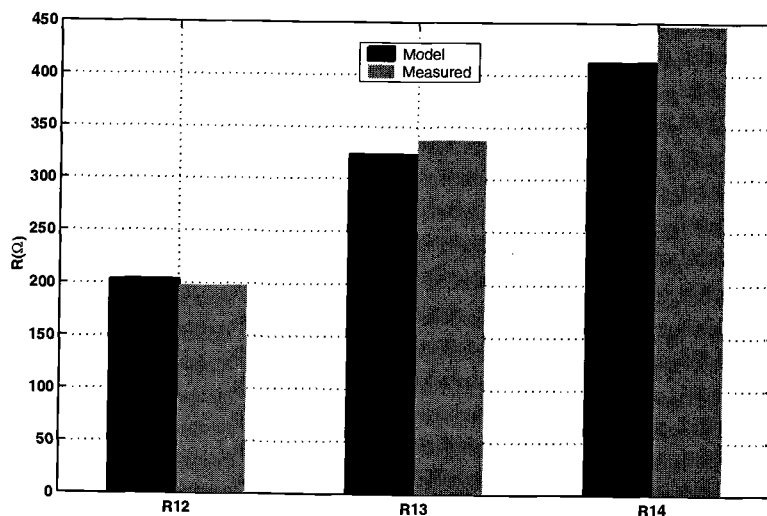


Figure 5.5. Comparison of measured resistance values with the model for the test structure shown in Fig. 5.3.

the array structure 1 in Table 5.1 shows that the value of resistance R_{1-2} increases drastically as the width of the contact is decreased. MEDICI simulations, however, do not reflect this behavior. A change in the width of the contact shows a very small change in the substrate resistance value. This is an expected result from 2D simulations. Figure 5.7 compares the measured value of R_{i-j} for the test structure shown in Fig. 5.6 with that calculated using the model. Good agreement between the model and the measured resistances is seen which further validates the accuracy of the model.

Test array 3 has three sets of contacts each of size $5\mu m \times 5\mu m$ at various separations as shown in Fig. 5.8. Table 5.3 shows the comparison between measured data and resistance values extracted from simulations. It can be seen that results

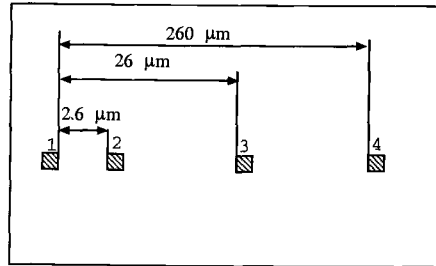


Figure 5.6. Array structure of $0.88\mu m \times 0.88\mu m$ contacts.

from EPIC and SCA show good agreement with the measured data. Shown in Fig. 5.9 is a comparison of the the measured data and the resistance values extracted using the model.

Table 5.2. Comparison of resistance values from 2D and 3D simulators with measured data for the test array shown in Fig. 5.6.

Resistances	Measured ($K\Omega$)	MEDICI ($K\Omega$)	SCA ($K\Omega$)	EPIC (Ω)	Model ($K\Omega$)
R_{1-2}	2.93	3	2.7	510	2.52
R_{1-3}	3.09	12	3.07	611	2.75
R_{1-4}	3.2	73.4	3.14	630	2.86

Test array 4 also has three sets of contacts each of size $5\mu m \times 5\mu m$ at various separations as shown in Fig. 5.10. Table 5.4 shows the comparison between measured data and resistance values extracted from simulations. It can be seen that results

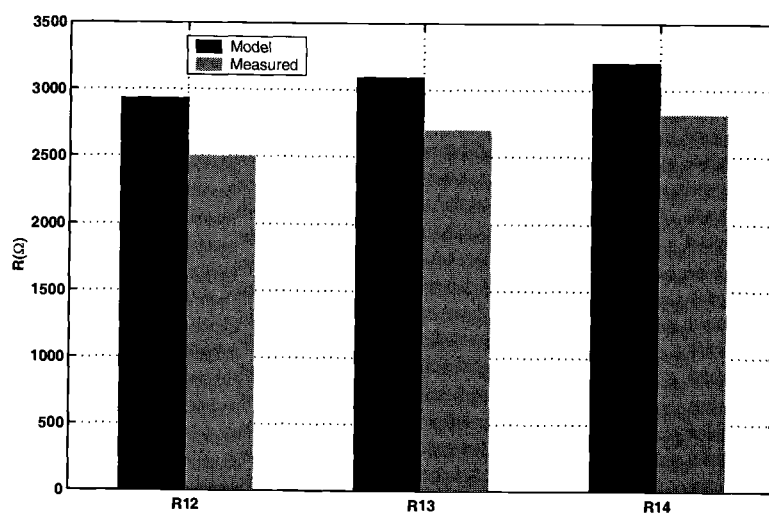


Figure 5.7. Comparison of measured resistance values with the model for the test array shown in Fig. 5.6.

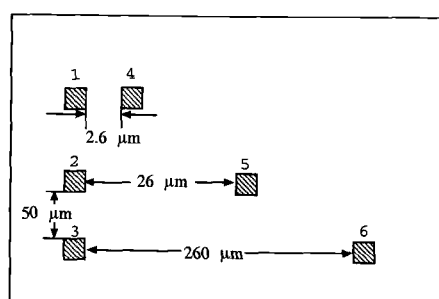


Figure 5.8. Test structure 3 of $5\mu\text{m} \times 5\mu\text{m}$ contacts.

from EPIC and SCA show a good agreement with the measured data. Shown in Fig. 5.11 is a comparison of the the measured data and the resistance values extracted using the model.

Table 5.3. Comparison of resistance values from 2D and 3D simulators with measured data for the test structure shown in Fig. 5.8.

Resistances	Measured (Ω)	MEDICI ($K\Omega$)	SCA (Ω)	EPIC (Ω)	Model (Ω)
R_{1-4}	203.5	2.29	196	182	183
R_{2-5}	326.5	12	306	304	300
R_{3-6}	414.65	73.4	450	441	375

Table 5.4. Comparison of resistance values from 2D and 3D simulators with measured data for the test structure shown in Fig. 5.10.

Resistances	Measured (Ω)	MEDICI ($K\Omega$)	SCA (Ω)	EPIC (Ω)	Model (Ω)
R_{1-4}	309.7	8.6	310	294	268
R_{2-5}	362.7	17.3	360	339	320
R_{3-6}	412.4	41.1	457	451	395

It can be concluded from the results shown in Figs. 5.5, 5.7, 5.9 and 5.11 that the model predicts the measured value accurately.

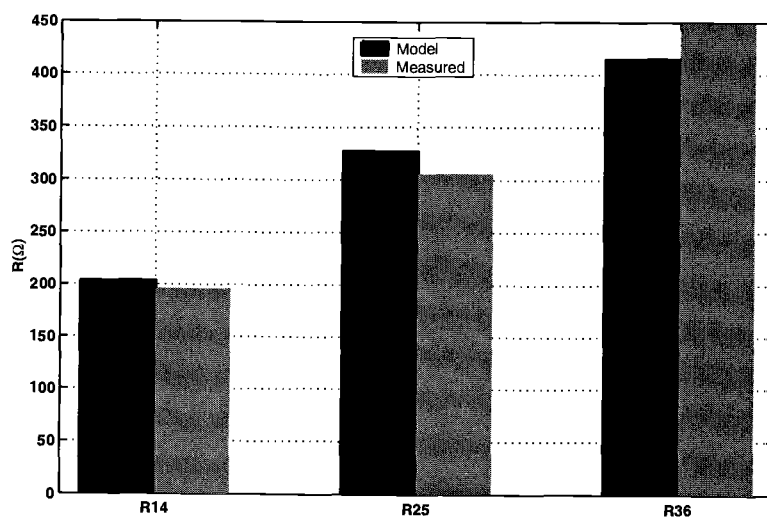


Figure 5.9. Comparison of measured resistance values with the model for the test structure shown in Fig. 5.8.

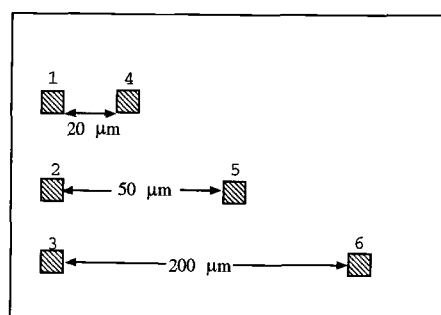


Figure 5.10. Test structure 4 of $5\mu m \times 5\mu m$ contacts.

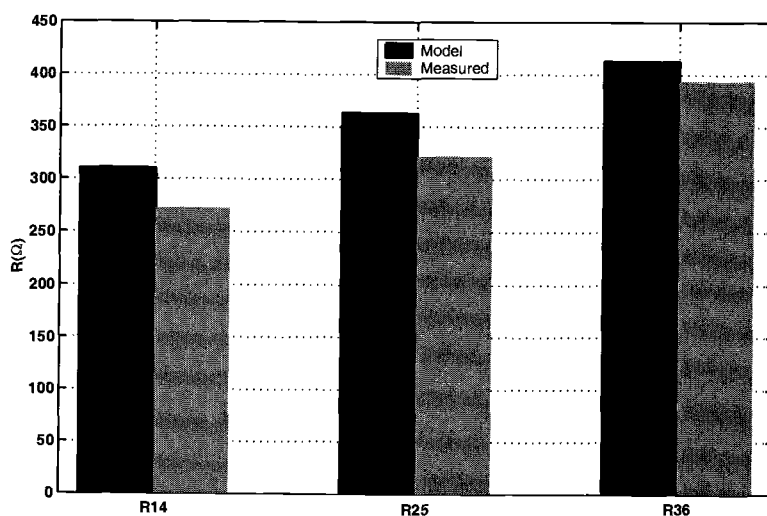


Figure 5.11. Comparison of measured resistance values with model for the test structure shown in Fig. 5.10.

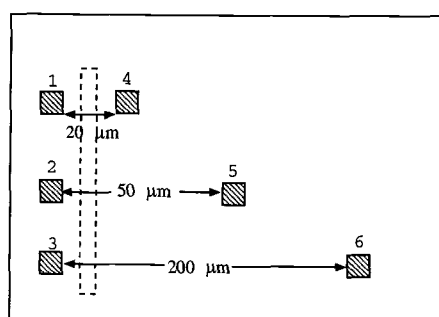


Figure 5.12. Test structure 5 of $5\mu\text{m} \times 5\mu\text{m}$ contacts.

Test array 5 also has three sets of two contacts each of $5\mu m \times 5\mu m$ size at various separations as shown in Fig. 5.12 but has a strip which does not have the conductive buried layer shown by the dotted line between the contacts. This structure could not be simulated using EPIC since only homogeneous substrate layers can be defined in EPIC. The resistance obtained from MEDICI and SCA are tabulated in Table 5.5. A comparison of the data in Table 5.4 and Table 5.5 shows that the resistance increases due to the strip of substrate without the buried layer between the contacts (Fig. 5.12).

Table 5.5. Comparison of resistance values from 2D and 3D simulators with measured data for the test structure shown in Fig. 5.12.

Resistances	Measured (Ω)	SCA (Ω)	MEDICI ($K\Omega$)
R_{1-4}	429.35	426	10.3
R_{2-5}	436.5	429.7	20.14
R_{3-6}	464.94	450.2	48.7

6. TECHNIQUES FOR IMPROVING ISOLATION

Some of the techniques used to improve isolation include increasing the separation between the injecting and the sensing contacts and using P+ guard rings or N-well isolation structures. Isolation is defined as the ratio of the open circuit voltage at the sensor to the voltage applied at the injecting contact.

$$Isolation = 20\log\left(\frac{V_{sensor}}{V_{injector}}\right)dB \quad (6.1)$$

In a lightly doped substrate, the maximum coupling takes place on the surface of the substrate because of the lower resistance at the surface as compared to the high resistivity bulk. For this reason, increasing the separation between the noise injecting source and the sensing circuit does not improve the isolation.

The effect of separation on isolation is shown in Fig. 6.1. At $x = 10\mu m$, the isolation was found to be -1.7 dB with an increase of the separation to $60\mu m$, the isolation was calculated to be -7.63 dB. Therefore, it can be seen that the separation between the injector and sensor does not reduce the noise coupling. Due to the

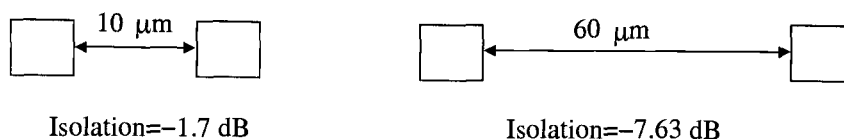


Figure 6.1. The effect of separation between injector and sensor on the isolation.

surface conduction in lightly doped substrates, the use of guard rings or substrate taps should be more effective in improving the isolation. The simulation setup used

to obtain the value of isolation in MEDICI is shown in Fig. 6.2. In this setup, the injector, sensor and the guard ring are all point contacts of $0.5\mu m$ width. When a grounded guard ring is placed between the injector and sensor, the guard ring picks up most of the injected noise. This effect is illustrated in Fig. 6.3 which shows that most of the current flows from the injector into the guard ring, thereby shielding the sensor.

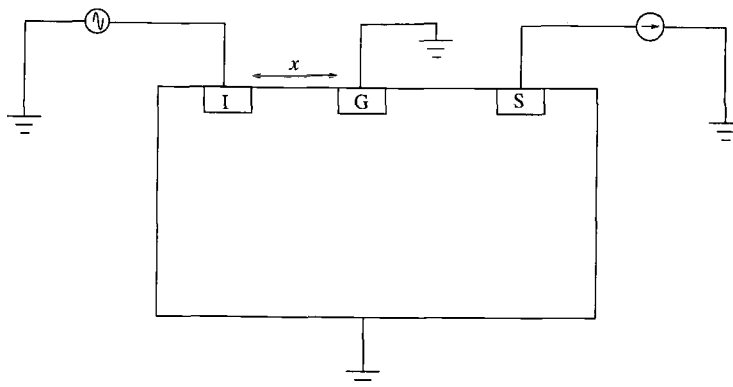


Figure 6.2. Simulation setup to determine isolation.

The plot in Fig. 6.4 was obtained by keeping the separation between the injector and sensor fixed at $60\mu m$ and varying the separation x between the injector and guard ring. Figure 6.4 shows that the isolation improves significantly due to the presence of the guard ring and that as the guard ring G is moved closer to the sensor, the isolation improves.

In order to improve the isolation further, the use of dual guard rings is examined. Since the isolation is maximum when the guard ring is closest to the sensor,

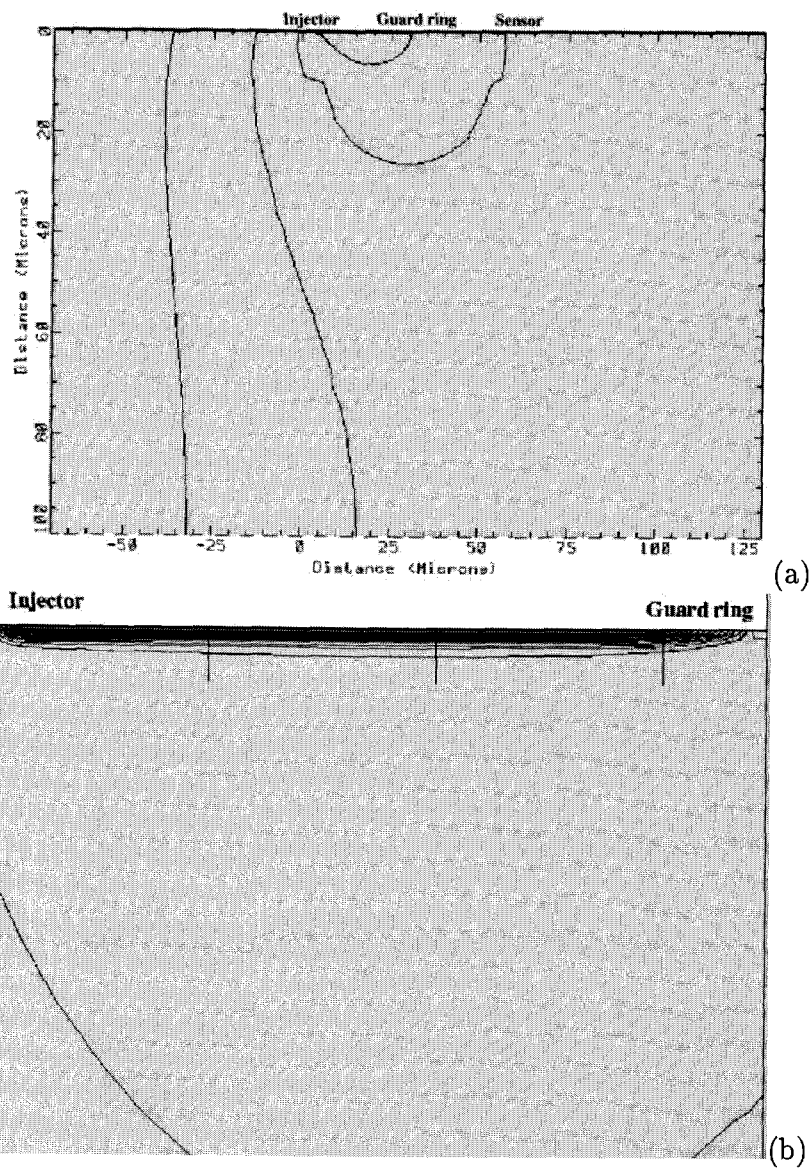


Figure 6.3. Current flow lines in a lightly doped substrate when:
(a) a guard ring is placed between the injector and the sensor.
(b) closer view of current flow lines.

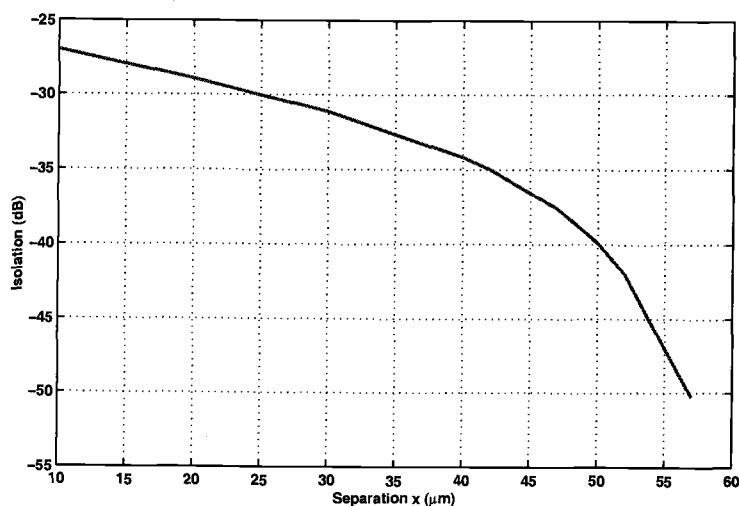


Figure 6.4. Isolation versus separation x with the guard ring and backplane grounded.

the guard ring $G1$ is fixed at a separation of $5\mu\text{m}$ from the sensor and the separation between the injector and sensor is $60\mu\text{m}$ as shown in Fig. 6.5. The second guard ring $G2$ is swept from $x = 10\mu\text{m}$ to $55\mu\text{m}$ and the results are plotted in Fig. 6.6. It can be concluded from Fig. 6.6 that the presence of $G2$ only improves the isolation as it is moved very close to the sensor S . The maximum isolation obtained with two guard rings placed between the noise injecting source and sensor is -61 dB .

Another dual guard rings setup is shown in Fig. 6.7 where the two guard rings are placed around the sensor. The guard ring $G1$ is fixed at a separation of $55\mu\text{m}$ from the injector while the separation between the injector and sensor is $60\mu\text{m}$. The second guard ring $G2$ is placed on the other side of the sensor to completely isolate the sensor as shown in Fig. 6.7. Figure 6.8 shows that the best isolation is obtained

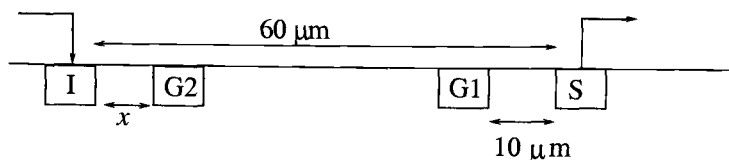


Figure 6.5. Setup with two guard rings.

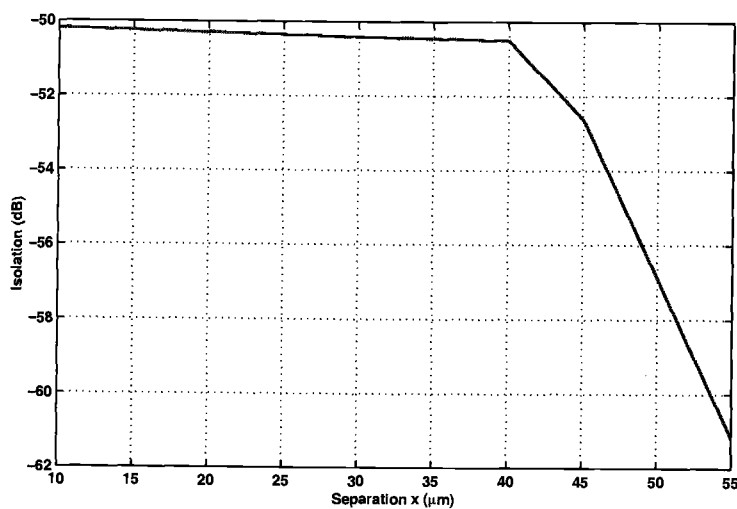


Figure 6.6. Isolation versus separation x with the guard rings and backplane grounded for the structure shown in Fig. 6.5.

when $G2$ is closest to the sensor. The maximum value of isolation obtained with this setup is about -69 dB.

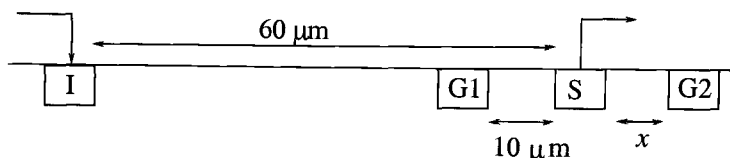


Figure 6.7. Setup with two guard rings around the sensor.

Next, the effect of the width of the guard ring on isolation is considered. The separation between the injector and the sensor is fixed at $60\ \mu\text{m}$ and the separation between the injector and the guard ring at $10\ \mu\text{m}$ as shown in Fig. 6.9. Now, varying the width, w , of the guard ring from $1\ \mu\text{m}$ to $50\ \mu\text{m}$, the plot in Fig. 6.10 is obtained. As the width of the guard ring is increased, the guard ring picks up more current from the injector thereby improving the isolation.

Up to this point, a perfectly grounded backplane and guard ring were considered. In reality, there is usually pin inductance involved. Here, the effect of the backplane connected directly to ground and through pin inductances is studied. Figure 6.11 shows the effect of connecting the guard ring to ground through pin inductances at various frequencies. At frequencies less than $1\ \text{GHz}$, there is no difference in isolation with and without an inductor to ground. At higher frequencies, however, the presence of the inductive impedance degrades the isolation between the injector and the sensor.

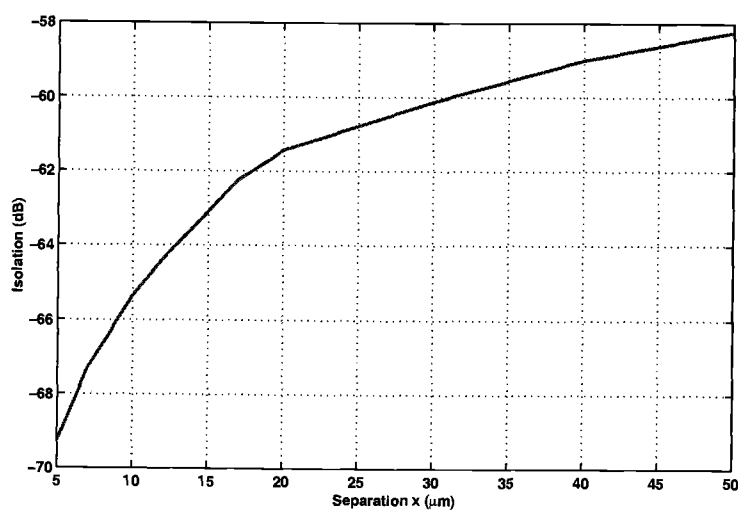


Figure 6.8. Isolation versus separation x with the guard rings and backplane grounded for the structure shown in Fig. 6.7.

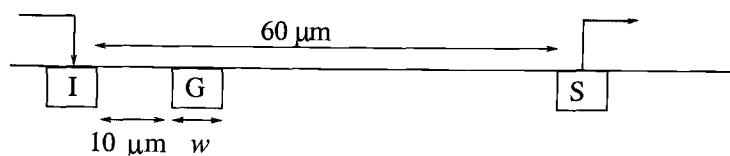


Figure 6.9. Simulation setup used to evaluate the effect of the width of the guard ring on isolation.

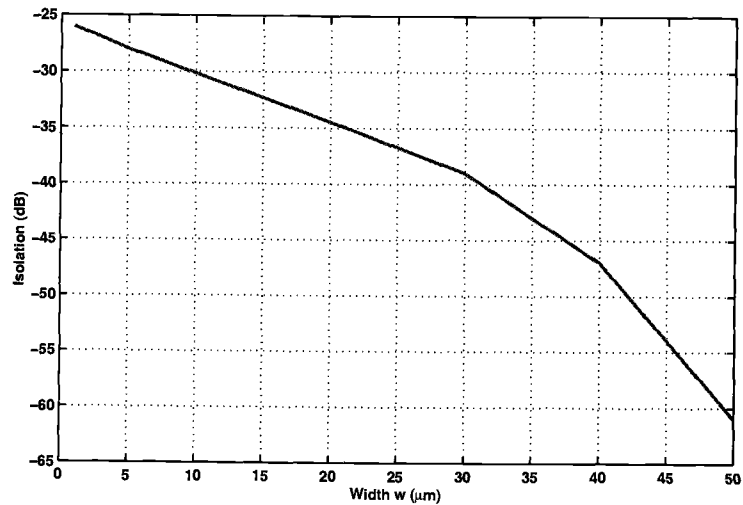


Figure 6.10. Isolation versus width W of the guard ring.

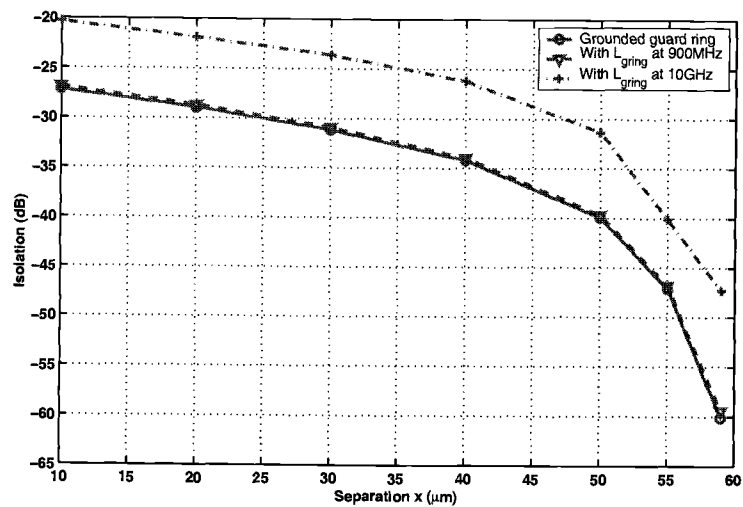


Figure 6.11. Comparison of isolation obtained while using a grounded guard ring and guard ring with inductive impedance at different frequencies.

Figure 6.12 shows a comparison of isolation obtained with a floating backplane, grounded backplane and with an inductive impedance of $5nH$ for the backplane at different frequencies. Here, again, at low frequencies, the presence of the inductive impedance does not affect the isolation value whereas at higher frequencies, there is a significant degradation in the value of isolation between the injector and sensor. As expected, a floating backplane degrades the isolation obtained.

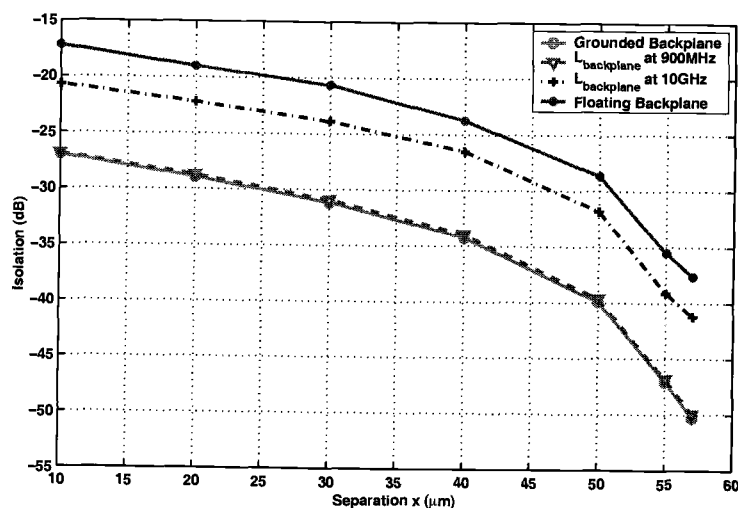


Figure 6.12. Comparison of isolation obtained while using a floating backplane, grounded backplane and pin inductance are shown.

It can be summarized that although placing the guard ring close to the sensor improves the isolation, it is the use of dual guard rings around the sensor that effectively shields the sensor from the noise injected into the substrate. If the pin inductances are large, there is a degradation in the isolation obtained. Therefore,

care must be taken to keep these inductances to a minimum for the guard rings to be effective.

7. COMPARISON OF LIGHTLY DOPED AND HEAVILY DOPED PROCESSES

In this chapter the behavior of heavily doped substrates is examined and compared with that of a lightly doped substrate. Figures 7.1 and 7.2 show the cross sections of a lightly doped substrate and a heavily doped substrate. A lightly doped substrate has a heavily doped P+ channel-stop implant layer and a lightly doped bulk whereas a heavily doped substrate has a heavily doped P+ layer, a more lightly doped epi layer and a heavily doped bulk. The resistance model for two

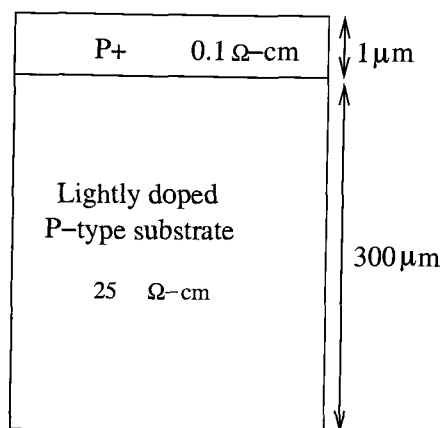


Figure 7.1. Cross-section of a lightly doped substrate without a buried layer.

contacts for both the processes is shown in Fig. 7.3. When the two contacts are of the same size, the vertical resistances R_{11} and R_{12} are equal. The resistance network for a lightly doped and heavily doped substrate for different values of separation x between contacts of $1\mu m \times 1\mu m$ is tabulated in Table 7.1.

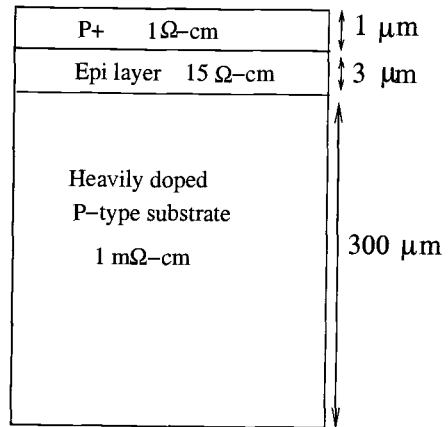


Figure 7.2. Cross-section of a heavily doped substrate.

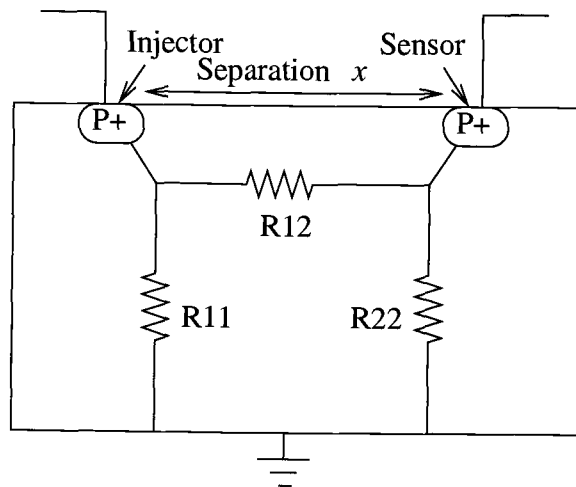


Figure 7.3. Resistive model of a lightly/heavily doped substrate.

Table 7.1. Resistance values obtained from MEDICI simulations for lightly doped and heavily doped processes.

Separation (μm)	R_{11} (K Ω)		R_{12} (K Ω)	
	Lightly Doped	Heavily Doped	Lightly Doped	Heavily Doped
10	897	143	3.76	162
20	582	121	5.6	187
30	518	103	8.2	219
40	368	96	10.04	253
50	286	91.2	12.54	287
60	265	85	15.13	320
70	238	81	17.3	353
80	219	77	20.41	385
90	195	75	23.12	416

A comparison of the data shown in Table 7.1 shows that R_{11} is much greater than the value of R_{12} for a lightly doped substrate. Therefore, most of the current flows through the surface of the substrate into the sensor. However, in a heavily doped substrate, the cross coupling resistance R_{12} is much higher than the vertical resistance R_{11} . This causes most of the injected current to flow through the bulk into the grounded backplane, thereby reducing the noise getting coupled into the sensor.

Table 7.2. Comparison of isolation values obtained for different processes.

Separation (μm)	Isolation (dB)	
	Lightly Doped	Heavily Doped
10	-1.7	-7.2
15	-2.4	-10.88
20	-3.14	-14.31
25	-3.79	-17.63
30	-4.4	-20.85
35	-4.9	-23.93
40	-5.55	-26.84
45	-6.08	-29.56
50	-6.94	-33.7
55	-7.08	-34.32
60	-7.63	-36.7

Table 7.2 shows the variation of isolation with separation for the two processes. It can be seen that isolation improves with separation significantly for a heavily doped process as compared to a lightly doped process. This further validates the behavior of the substrate as explained earlier in terms of current flow.

If the backplane is not grounded, the effective resistance between the injector and sensor is the value of R_{11} in parallel with R_{12} which is a small number. Therefore, the noise coupling into the sensor increases drastically when the backplane is left floating in a heavily doped substrate. In a lightly doped substrate also, a floating backplane increases the noise coupling into the sensor though not as significantly. However, the use of guard rings (discussed in Chapter 6) helps reduce the noise getting coupled into the sensor in a lightly doped substrate.

Therefore, it can be concluded that the noise coupling into the sensor in a heavily doped substrate is considerably less than that in a lightly doped substrate when the backplane is grounded. A floating backplane, however, can increase the sensed noise significantly which can be reduced using guard rings in a lightly doped process.

8. CONCLUSION

A macromodel for substrate noise coupling between multiple contacts in two lightly doped processes has been developed . This model is efficient, accurate and is scalable with the size and separation between the contacts. The model has been validated with measured results and simulations. The model is simple and requires a few parameters to be extracted. Once the parameters are known for the particular process, the model can be used to extract the substrate model for any situation before layout. The improvement in isolation by the use of guard rings has also been investigated.

Future work should focus on extending the macromodel to higher frequencies when the substrate can no longer be modeled as a simple resistive network. The model can be incorporated in a CAD tool to automate the process of extracting the substrate network for circuit examples.

BIBLIOGRAPHY

- [1] M. Ingels and M. S. J. Steyert, "Design strategies and decoupling techniques for reducing the effects of electrical interference in mixed-mode IC," *IEEE journal of Solid-State Circuits*, vol. 32, pp. 1136-1141, July 1997.
- [2] K. Makie-Fukuda, S. Maeda, T. Tsukada and T. Matsuura, "Substrate noise reduction using active guard band filters in mixed-signal integrated circuits," *Symposium on VLSI Circuits Digest of Technical Papers*, pp. 33-34, June 1995.
- [3] W. W. T. Chan, J. K. O. Sin and S. S. Wong, "An effective cross-talk isolation structure for power IC applications," *IEDM*, pp. 38.4.1-38.4.4, December 1995.
- [4] P. Basedau and Q. Huang, "A post processing method for reducing substrate coupling in mixed-signal integrated circuits," *Symposium on VLSI Circuits Digest of Technical Papers*, pp. 41-42, June 1995.
- [5] R. Gharpurey and R. G. Meyer, "Modeling and analysis of substrate coupling in integrated circuits," *IEEE Journal of Solid-State Circuits*, vol. 31, pp. 344-352, March 1996.
- [6] N. K. Verghese, D. J. Allstot and M. A. Wolfe, "Fast parasitic extraction for substrate coupling in mixed-signal ICs," *IEEE Custom Integrated Circuits Conference*, pp. 121-124, May 1995.
- [7] R. Gharpurey, "Modeling and analysis of substrate coupling in integrated circuits," *Ph.D. Dissertation, Memo. No M95/47*, Electronics Research Laboratory, University of California, Berkeley, 1995.
- [8] A. Samavedam, A. Sadate, K. Mayaram and T. S. Fiez, "A scalable substrate noise coupling model for design of mixed-signal IC's," *IEEE Journal of Solid-State Circuits*, vol. 35, pp. 895-903, June 2000.
- [9] A. C. Sadate, "A substrate noise coupling model for lightly doped CMOS processes," M.S. Thesis, Oregon State University, December 2000.
- [10] H. Dicle Ozis, "An efficient modeling approach for substrate noise coupling analysis with multiple contacts in heavily doped CMOS processes," M.S. Thesis, Oregon State University, August 2001.
- [11] A. J. Van Genderen and N. P. Van der Meijs, "Modeling substrate coupling effects using a layout-to-circuit extraction program," *Proceedings of IEEE Benelux Workshop on Circuits, Systems and Signal Processing*, pp. 193-200, November 1997.

- [12] B. R. Stanisic, N. K. Verghese, R. A. Rutenbar, L. R. Carley and D. J. Allstot, "Addressing substrate coupling in mixed-mode IC's: simulations and power distribution synthesis," *IEEE Journal of Solid-State Circuits*, vol. 29, pp. 226-238, March 1994.
- [13] I. L. Wemple and A. T. Yang, "Integrated circuit substrate coupling models based on Voronoi-tessellation substrate macromodels," *IEEE Trans. Computer-Aided Design*, pp. 1459-1469, December 1995.
- [14] MEDICI, Version 2000.2.0, Avant! Corporation, 2000.
- [15] Affirma Substrate Coupling Analysis Version 4.4.5, Cadence Design Systems, Inc., December 1999.
- [16] C. G. Xu, "EPIC: A program for extraction of the resistance and capacitance of substrate with the Green's Function method," Oregon State University, 2001.
- [17] N. K. Verghese and D. J. Allstot, "Computer-aided design considerations for mixed-signal coupling in RF integrated circuits," *IEEE Journal of Solid-State Circuits*, vol. 33, pp. 314-323, March 1998.

APPENDICES

APPENDIX A. Model Parameter Extraction for Z_{11}

Z_{11} is measured for a single contact. It is the ratio of the open circuit voltage at the contact to the input current at the contact, with all other contacts as open circuits.

$$Z_{11} = \frac{V_1}{I_1} \quad (A1)$$

Z_{11} can be modeled as a function of the contact area and perimeter.

$$Z_{11} = \frac{1}{A + B \times Area + C \times Perim} \quad (A2)$$

Parameters to extract: $A(\frac{1}{\Omega})$, $B(\frac{1}{\Omega m^2})$ and $C(\frac{1}{\Omega m})$. These parameters are constant for a given substrate.

Objective: To calculate Z_{11} for any contact size in a given substrate using the extracted parameters.

Parameter Extraction Steps:

- **Step 1:** Obtain at least 10 different data points (from simulations or measurements) for Z_{11} using a single contact with both square and rectangular geometries. Vary contact sizes in the range of $2.4\mu m$ to $50\mu m$.
- **Step 2:** Extract parameters A , B and C by curve-fitting (A2) to Z_{11} data.

```
%Curve fitting for Z11

clear all;

close all;

load Z11.dat;

area=Z11(:,1);

perim=Z11(:,2);

Z11=1./Z11(:,3);


options(2)=1e-10;

options(3)=1e-10;

options(6)=2;

options(7)=1;

options(14)=50000;


lam=fmins('fitZ11',[0,0,0],options,[],area,perim,Z11);


A=lam(1);

B=lam(2);

C=lam(3);

z11_model= (A*B*(Area)+C*(perim));

grid on

error=100*abs(z11_model-Z11)./Z11;

figure(1)

plot(area,z11_model,area,Z11,'ro');
```

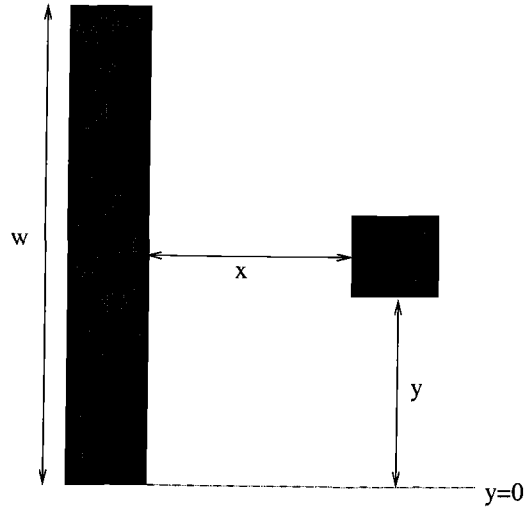
```
legend('Model','Simulation')
xlabel('Area of contact (sq um)')
ylabel('Z11 (ohm)')

figure(2)
plot(area,error)
xlabel('Area of contact (sq um)')
ylabel('Percentage Error ')

% Error calculation between simulated data and the model function.
function [error_data]=fitZ11(lam,area,perim,Z11)
global errvec;
global count;
error = Z11-(lam(1)+lam(2)*Area+lam(3)*Perim);
error_data=norm(error);
errvec(count)=error_data;
count = count+1;
```

APPENDIX B. Model Parameter Extraction for Z_{12}

$Z_{12}(x, y)$ is a function of x , y and the dimensions of the contacts, where x is the separation between the contacts and y is the relative position of the two contacts, as described below.



Z_{12} is measured for two contacts. It is the ratio of the open circuit voltage at the first contact to the input current at the second contact, with all other contacts as open circuits.

$$Z_{12} = \frac{V_1}{I_2} \Big|_{I_1=0}$$

PARAMETER EXTRACTION FLOW FOR Z_{12} (x dependence)

Z_{12} as a function of x can be modeled as

$$Z_{12} = \frac{\alpha e^{-\beta x}}{\epsilon + \sqrt{x}}$$

Parameter to extract: $\beta(\frac{1}{m})$. β is a constant for a given substrate.

Parameter to calculate: α ($\Omega\sqrt{m}$) and ϵ (\sqrt{m}). α and ϵ depend on contact dimensions.

Objective: To calculate Z_{12} for any contact size in a given substrate using extracted parameters.

Parameter Extraction Steps:

- **Step 1:** Obtain at least 10 different data points (from simulations or measurements) for Z_{12} using two contacts with square or rectangular geometries for different separations. First choose geometries in the range of $2.4\mu m$ to $50\mu m$ and then vary the separation from $10\mu m$ to $200\mu m$.
- **Step 2:** In order to obtain the values of α and ϵ , curve fit the Z_{12} data for different contact dimensions to the expression

$$\alpha = A + BP_{merged}$$

where P_{merged} is the perimeter when the two contacts are merged together, when $x = 0$. ϵ is also a linear function of P_{merged} given by:

$$\epsilon = C + DP_{merged}$$

The constants A ($\Omega\sqrt{m}$), B ($\frac{\Omega}{\sqrt{m}}$), C (\sqrt{m}), D ($\frac{1}{\sqrt{m}}$) are determined by curve fitting the values of α and ϵ to the equations shown above.

- **Step 3:** Using the Z_{12} data and the expression for $Z_{12} = \frac{\alpha e^{-\beta x}}{\epsilon + \sqrt{x}}$ curve fit to determine β .

PARAMETER EXTRACTION FLOW FOR Z_{12} (y dependence)

Z_{12} as a function of y can be modeled as

$$Z_{12} = ay^2 + by + c \quad (B1)$$

Parameters to extract:

- $a(\frac{\Omega}{m^2})$. a depends on contact dimensions as well as separation between contacts x .
- $c(\Omega)$. c also depends on contact dimensions.

Objective: To calculate Z_{12} for any contact size in a given substrate using extracted parameters.

Parameter Extraction Steps:

- **Step 1:** Choose contact geometries such that the length of one contact is larger than the other so that the smaller contact can be moved along the y -direction.
- **Step 2:** Calculate c by observing that $Z_{12}|_{y=0} = c$. Thus $c = \frac{\alpha e^{-\beta x}}{\epsilon + \sqrt{x}}$.
- **Step 3:** Now (B1) can be written as:

$$\frac{Z_{12}}{Z_{12}|_{y=0}} = \frac{Z_{12}}{c} = (a_1 y^2 + b_1 y + 1)$$

- **Step 4:** Determine a_1 by curve fitting Z_{12} data for different x values to the expression given by:

$$a_1 = (K_1 + K_2 x + K_3 \sqrt{x})$$

b_1 is related to a_1 as shown below:

$$\frac{b_1}{2} = \frac{-a_1 w}{2}$$

- **Step 5:** Once the parameters are extracted for a specific pair of contacts, they are applicable to any contact geometries since a_1 does not depend on contact dimensions.

```
% Curvefitting

close all;

load data_z12;
x=data_z12(:,1);
z12_sim=data_z12(:,3);

options(2)=1e-10;
options(3)=1e-10;
options(6)=2;
options(7)=1;
options(14)=100000;

lam=fmins('fitz12',[0,0,0],options,[],x,z12_10);
alpha=lam(1);
beta=lam(2);
epsilon=lam(3);
z12_model=(alpha*exp(-1*beta*x))./(epsilon+sqrt(x));
error=100*abs(z12_model-z12_sim)./z12_sim;

figure(1)
plot(x,z12_model,x,z12_sim,'ro');
legend('Model','SCA')
```

```

title('Z12 for 10uX10u contacts')
xlabel('Separation (um)')
ylabel('z12_sim (mho)')

figure(2)
plot(x,error)
title('Percentage error for 10uX10u contacts')
xlabel('Separation (um)')
ylabel('Percentage Error (mho)')

%Error Calculation between Simulation and Model
function [error_data]=fitz12(lam,y,z12)
global errvec;
global count;
error=z12-(lam(1)*exp(-1*lam(2)*x)./(lam(3)+sqrt(x)));
error_data=norm(error);
errvec(count)=error_data;
count = count+1;

% Curvefitting for Z12 dependence on y
close all;
clear all;
load diff_shap_y_data;
y=diff_shap_y_data(:,1);
z12_sim=diff_shap_y_data(:,3);

```

```

options(2)=1e-10;
options(3)=1e-10;
options(6)=2;
options(7)=1;
options(14)=100000;

lam=fmins('fitz12_diffshap_y',[0,0,0],options,[],x,z12_sim);
a=lam(1)
b=lam(2)
c=lam(3)

z12_model=a*(y.^2)+(b*y)+c
error=100*abs(z12_model-z12_sim)./z12_sim;

figure(1)
plot(x,z12_model,x,z12_sim,'ro');
legend('Model','SCA')
xlabel('Separation (um)')
ylabel('z12 ')

figure(2)
plot(x,error)
xlabel('Separation (um)')
ylabel('Percentage error')

```

```
%Error Calculation between Simulation and Model  
function [error_data]=fitz12(lam,y,z12)  
global errvec;  
global count;  
error=z12-(lam(1)*y.^2+lam(2)*y+lam(3));  
error_data=norm(error);  
errvec(count)=error_data;  
count = count+1;
```